Computational Investigation of the Ionization and Photo-Ionization of Hydrogen Halide Acids in Water Clusters

Sacha Z. Zlatkova

A Thesis

in

The Department

of

Chemistry and Biochemistry

Presented in Partial Fulfillment of the Requirements
for the Degree of Master of Science (Chemistry) at
Concordia University Montreal, Quebec, Canada

December, 2006

Your file Votre référence
ISBN: 978-0-494-28882-5
Our file Notre référence
ISBN: 978-0-494-28882-5

Abstract

Computational Investigation of the Ionization and Photo-Ionization of Hydrogen Halide Acids in Water Clusters

Sacha Z. Zlatkova

The ionization of hydrogen halide acids HX (X=Cl, Br) in the presence of water in the ground and excited electronic states is an important fundamental process, with possible implications for the ozone layer depletion. Experimental investigations of acid dissociation and hydration of ion pairs $[X^-(H_2O)_nH_3O^+]$ at the molecular level are hindered by instrument limitations, and to date, theoretical studies address the mechanism of acid ionization in polar and non-polar solvents only partially. This thesis aims at characterizing ground-state acid-water complexation and ionization, and possible effects of water on the ionization of HX in electronically excited states.

As for ground-state ionization, the structures of HCl and HBr in aqueous clusters of different sizes were characterized with second-order Møller-Plesset perturbation theory (MP2), and coupled cluster theory with single, double and perturbative triple excitations [CCSD(T)], paying particular attention to the critical number of water molecules needed for acid ionization to occur. Combined results from the quantum theory of atoms in molecules (AIM) and infrared (IR) vibrational spectra analyses are used to unambiguously characterize the nature of bonding in acid-water clusters. Global minimum-energy cluster structures suggest that both HCl and HBr form ionized complexes in the presence of four water molecules.

As for possible excited-state ionization of hydrogen halides, the excited-state electronic structures and potential energy curves of gas-phase HBr were first obtained from multi-reference configuration interaction (MRCI) calculations. Investigation of the influence of water molecules on the excited-state potential energy curves of HBr then revealed the feasibility of excited-state ionization, and thus photo-ionization in water clusters, due to opening of an ion-pair dissociation channel. This work thus claims the interpretation of recent experimental findings [Science, 2002], in which HBr photo-ionization was observed in small water clusters, but not for clusters larger than size 4, presumably because of ground-state ionization that quenches the HBr photo-ionization channel.

Acknowledgements

I would like to take this opportunity to thank my supervisor Dr. Gilles H. Peslherbe for his valuable advices and financial support in the process of my entire research work at Concordia University. His encouragement towards the challenges I faced along the last two years of scientific investigations and the opportunities he gave me to show our work on national level conferences and symposia are most valuable experience for my carrier.

Next I would like to thank the other two members of my committee Dr. Peter H. Bird and especially Dr. Heidi M. Muchall for the very interesting and stimulating questions on the annual committee meetings, which naturally contributed to the quality of my work.

I would like to thank all my colleagues and especially Qadir, Denise, Robert, Sean, Elena and Lei for the very productive discussions and help.

I am mostly grateful to my family, Dr. Boyko A. Dodov and our son Anton (Toni) for their constant moral support and belief in me.

To my son Anton.

Table of Contents

List of Figures

List of Tables

List of Abbreviations

AIM	Atoms in molecules
B3LYP	Beck's three-parameter exchange and Lee-Yang-Parr correlation hybrid functional
BCP	Bond critical point
BSSE	Basis set superposition error
CAS	Complete active space
CAS-SCF	Complete active space self-consistent field
CCSD(T)	Coupled clusters with single, double and perturbative triple excitations
CP	Counterpoise
ECP	Effective core potential
HB	Hydrogen bonding
HF	Hartree-Fock
IP	Ionization potential
IR	Infrared
MO	Molecular orbital
MP2	Second-order Møller-Plesset theory
MRCI	Multi-reference configuration interaction
PEC	Potential energy curve
PP	Pseudopotential
RCP	Ring critical point
VSCC	Valence shell charge concentration
ZPE	Zero-point vibrational energy

Chapter I.

General Introduction

I.1. Hydrogen Halides Acid Chemistry

Strong acids such as hydrogen halides are present and play an important role in many processes in a large variety of living and non-living systems on our planet. When dissolved in water under ambient conditions, acids dissociate into ions, common knowledge in modern science, but a revolutionary discovery explained by the Arrhenius dissociation theory back in the late eighties of the nineteenth century [1, 2]. As knowledge advances and a more sophisticated understanding emerges about matter and its structure, this theory must be extended to a wider temperature range and to systems where more types of molecular interactions are involved. In living organisms, ions from dissociated hydrogen halides (mostly HCl and HBr, but also HF and HI) play an important role in the proper functioning of e.g. gastro-internal systems, ion-channels of cell membranes, enzyme catalysis, drugs, etc. A very recent review of halogen-containing biochemical systems [3] describes their important features. For example, Walsh's research group has been working extensively for many years to reveal the mechanism of halogenation by enzyme, in order to characterize their catalytic activity and design strategies for the halogenation to other substrates. Halogenation leads to alteration of the enzyme physical properties, such as the electronic and steric effects that may govern the affinity and selectivity of ligand-substrate complexes, as observed for the binding interaction of chlorinated antibiotic vancomycin to its cell-wall target [4].

Hydrobromic and hydrochloric acid are widely known as chemical products released in the atmosphere resulting from industrial processes and naturally from volcanic activity. It is arguable which of the above factors most significantly influenced and/or triggered the current climate changes, nonetheless it was unambiguously proven

that chlorofluorocarbons (CFC), chlorofluoromethanes (CFM), halones, as well as a series of other industrial wastes, participate in atmospheric chemical processes, resulting in the destruction of the UV-protecting ozone layer, severe weather changes, and agricultural issues, which all may endanger the future of our planet. Even though a very recent sign of relief comes from the conclusion of Weatherhead and Andersen [5] that the ozone layer has stopped depleting, and is locally recovering, the authors are implicitly warning that it is unlikely we will observe full recovery of the ozone layer, and that its instability is a result of the chemical content of the polar stratospheric clouds (PSCs) formed during very cold seasons. The latter are formed of aerosol particles and ice crystals during the Antarctic winter at temperatures of about 180-190 K [6]. Hydrogen halides are most probably adsorbed on the surface of these ice-water crystals or droplets, constituting a system known as an acid-water cluster. It is believed that these clusters play a key role in the mechanism of formation of halide radicals [7, 8], which leads to ozone destruction via a complex sequence of chemical reactions upon photoexcitation.

The 1995 Nobel Prize in chemistry was shared by Paul Crutzen, Mario Molina, and Sherwood Rowland for their pioneering contributions [9-11] in explaining the mechanisms of the ozone layer formation and depletion, and emphasizing the connection of a particular group of chemicals of anthropogenic origin present in the atmosphere to the ozone loss phenomenon. The chemical processes and kinetics affecting stratospheric ozone depletion have been reviewed in detail [8, 12, 13]. The lowest atmospheric layer - the troposphere spans from the surface to about 10 km in altitude. Since the temperature and pressure gradually decrease with altitude, the dynamics of tropospheric air masses is characterized mostly by a convection motion, carrying up all anthropogenic and natural

chemical waste. At an altitude between 7 and 10 km, in the tropopause, at temperatures around 210 K, these chemical compounds start to aggregate or mix with water in the form of ice crystals. The chemistry of CFC/Halon replacement compounds takes place in this part of the atmosphere [14]. Above the tropopause, up to 50 km spans the stratosphere, which is characterized with a gradual increase in temperature and motion of the air masses is mostly horizontal, contributing to a large spread of these industrial and volcanic chemicals. Heterogeneous processes, involving fluorine, bromine, and iodine species and occurring on acid-aerosol particles, characterize the stratospheric chemistry. The increase in the stratospheric temperature is a result of the energy released from the solar photolysis of stratospheric species such as ozone. In a normal situation, in the moderate presence of industrial chemicals and regular atmospheric gases, UV-radiated oxygen molecules (O_2) dissociate into atomic oxygen radicals ($O\bullet$), which instantly react back with O_2, producing ozone (O_3). This is a photocycle since photolysis also proceeds backwards leading to self-destruction of ozone molecules (a very slow process - O_3 has 1 to10 years lifetime). Therefore, in these ideal conditions, the ozone layer thickness varies only slightly (within 3 km) depending on the solar radiation and atmospheric air dynamics. However, it was firmly established that chlorofluorocarbons (CFC), halones and other green-house gases act as catalysts for the reversed reaction, and therefore significantly affect the stability of the ozone layer.

One of the most widely accepted mechanisms for ozone destruction beyond its normal regeneration cycle involves the following reactions:

$$Cl + O_3 \rightarrow ClO \qquad (1)$$

$$ClO + O \rightarrow Cl + O_2 \qquad (2)$$

$$ClO + NO \rightarrow Cl + NO_2 \qquad (3)$$

In the stratosphere, Cl radicals react readily with various hydrogen-containing species to form HCl. Kinetics studies [7] have shown that the largest rate coefficients of formation of HCl are from reactions with CH_4 (10^{-3} $cm^{-3}s^{-1}$), although H_2O_2 and HNO_3 also contribute (~10^{-5} $cm^{-3}s^{-1}$ and ~10^{-6} $cm^{-3}s^{-1}$, respectively). A similar mechanism applies to BrO_x (x = 1,2) for the formation of hydrobromic acid (HBr), with the significant difference that BrO_x species are much more thermodynamically unstable than ClO_x [15], and at the same time bromine species have a higher destructive potential for ozone than their chlorine analogs. The above gas-phase mechanism would lead to accumulation of Cl mostly in the form of hydrochloric acid (HCl) and chlorine nitrate ($ClONO_2$), but despite their high reactivity, Cl radicals are not the direct cause for the ozone depletion via a simple gas-phase mechanism. While this gas-phase chemistry only provides a partial explanation of the exact mechanism of hydrogen halide ozone destruction rule, an alternative, heterogeneous chemistry approach, initially proposed by Solomon et al. [16], complements it by the following reaction:

$$ClONO_2 + HCl \rightarrow HNO_3 + Cl_2 \qquad (4)$$

Later, Hynes and co-workers [17-20] in series of publications explained the possible outcomes of this reaction. Firstly, according to the hypothesis for heterogeneous origin of Cl radicals, reaction (4) takes place on the ice surface of polar stratospheric aerosol particles, therefore the possibility for it to be a two-step mechanism has to be explored. The former involves hydrolysis of the chlorine nitrate to produce hypochlorous acid (HOCl), which on a second step reacts with the HCl to produce Cl_2:

$$ClONO_2 + H_2O \rightarrow HNO_3 + HOCl \qquad (5)$$

$$HOCl + HCl \rightarrow H_2O + Cl_2 \qquad (6)$$

Molecular chlorine (and, as later also established, bromine) is then photolyzed during the Antarctic spring, to form halide radicals, which as explained earlier in this chapter act as catalyst for the destructive part of the ozone cycle. Experimental and subsequent theoretical studies provide an important finding: the water network of the ice surface provides not merely a platform but is an important reagent, which facilitates the rapid hydrolysis of chlorine nitrate. A barrier of 30 kcal/mol was estimated for reaction (4) in the absence of water, but three water molecules are able to catalyze the reaction through a proton shuttle mechanism [19].

The two-step mechanism of Cl_2 and Br_2 production was experimentally and theoretically excluded, because it was proven [20, 21] that the product from reaction (5), nitric acid (HNO_3), slows down the hydrolysis substantially by acidifying the ice surface. Moreover, the ionization of HCl by water and subsequent proton transfer appear to be the most likely path for reaction (4). At this point, the investigation of this mechanism, experimentally and theoretically, fall into several categories of studies: ionization of hydrogen halides in the presence of $XONO_2$, (X = Cl, Br) on ice surfaces, or ionization of hydrogen halides in water clusters, on ice surfaces, or in the liquid phase. An overview of the results obtained previously for the ionization of HCl and HBr in water clusters follows.

I.2. Experimental Studies of HCl and HBr Ionization

It is now widely accepted that the key step in the mechanism of polar ozone depletion involves the interaction of HCl and HBr with the particles that constitute polar stratospheric clouds. The characteristic temperature of these systems is below approximately 185 K. Experimental work to investigate the mechanism of reaction (4) includes studies of the interaction of HCl and $ClONO_2$ on an ice surface, as well as studies of HCl –water clusters. Direct observation of HCl and HBr remains difficult due to the technical challenges of performing experiments with molecular specificity under the conditions typical of the polar stratosphere (~ 10^{-4} Torr and 180 K), for which traditional surface-science techniques, which require ultra-high vacuum conditions, are often not suitable. Thus, it is still not known whether HCl/HBr exists in an ionic or molecular form at (or near) the ice surface. Spectroscopic evidence [22, 23] indicates an ionic form of HCl at low temperatures (less than 180 K) and partial pressures where ionic hydrates of HCl are known to be thermodynamically stable [24]. However, some experimental studies suggest, that HCl is absorbed in molecular form [25, 26]. Estimates of the HCl-ice interaction energy has been reported, but the many assumptions employed, and the poor reproduction of the exact conditions of the polar stratosphere make these results not fully reliable. For example, in a beam study [26], the binding energy of HCl on a slowly condensing ice at 165 K was estimated to be 31 – 38 kJ/mol (7.4 – 9.1 kcal/mol), whereas an interaction energy of 25 kJ/mol (6.0 kcal/mol) was determined for HCl with a slowly evaporating HCl-covered ice. In two other beam studies on the desorption of HCl by an amorphous ice surface held at 100 – 126 K, an activation energy of desorption of 30 – 26 kJ/mol (7.2 – 6.2 kcal/mol) was estimated, while for a

temperature regime 140 K, a value of 33 ± 5 kJ/mol (6.7 – 9.1 kcal /mol) was reported [27]. All these uncertainties in the energy of formation of the HCl-ice lattice complexes require a theoretical investigation of the absorption-desorption process.

Initial ground-state charge separation in simple acids like HBr and HCl has been predicted to occur upon contact with as little as four water molecules [28, 29]. In several experimental cluster studies, it was determined that a diamond-like ionized complex in which Br^- and H_3O^+ are separated by three more water molecules exists for the smallest ice monocrystals of pure water [30], and of water bound independently to the hydronium [31] and bromide [32] ion. As mentioned earlier, experiments indicate that the uptake of HBr [33] by ice exceeds that of HCl, due to different dissociation abilities. In a recent experiment, Hurley et al. [34] demonstrated charge separation in size-selected $HBr{\cdot}(H_2O)_n$ clusters. Neutral clusters of HBr with water serve as chromophores for resonant multiphoton ionization, and they would form easily detectable cationic cluster products. Upon dissociation of this complex into Br^- and H_3O^+, the chromophore species disappear, eliminating the photoionization pathway and the cation signal altogether. Experiments showed that the signal disappears upon addition of the fifth water molecule, which led the authors to the conclusion that HBr needs to form a five-water cluster in order to undergo ground-state ionization. However, it was also mentioned that the temperature of this experiment cannot be precisely determined and therefore a strict conclusion about the mechanism of HBr ionization in water cannot be made. The experimental results reported so far give a relatively good basis to support the hypothesis of the mechanism of ozone depletion through acid dissociation, but technical limitations

of the experimental setups and the complexity of the system and conditions, all warrant a thorough theoretical investigation.

I.3. Theoretical Studies of HCl and HBr Ionization

Computational work to study the interaction of acids with the ice surface of PSC particles and in water clusters (which serve as a suitable model to investigate the mechanism of acid dissociation at the molecular level) is scattered, and only a review of the key studies will be given here. Theoretical investigations of acid dissociation in water have focused on: (a) the evolution of the acid-water system in time [27, 35-38] or (b) quantum chemical properties, such as the energy of formation, dipole moments, infrared vibrational frequencies and geometrical parameters of ionized and non-ionized clusters [28, 39-44].

Geometrical parameter and energetics of HX-water have been reported for halide series (X=F, Cl, Br, I) [24, 28, 40, 42-46]. In a comprehensive investigation of the ionization state of HCl in clusters containing up to three waters [39] it was shown that the most stable conformation is a hydrogen bonded, where HCl acts as a proton donor. The H_{acid}-Cl interaction was qualified as non-hydrogen bonding which stabilizes the ring structure of the cluster [39]. In addition, the very large red shift observed in the stretching frequency of HCl and the symmetric stretching mode of the donor O-H_{water} were ascribed to the hydrogen-bond formation. Based on the increase in the HCl bond length, charge transfer within the O···HCl hydrogen bond and stretching frequency changes, the authors concluded that the HCl bond strength decreases although HCl is not ionized. Studies of four- water clusters of hydrogen halides [43, 46-48] indicate that HCl and HF form fully

ionized stable complexes, where stabilization arises solely from the six hydrogen bonds formed. Specifically for HCl, a minimum of four water molecules is required in order to form stable structures, in which positive and negative ions coexist in the cluster, with a binding energy of 41.2 kcal/mol as estimated with density-functional theory [47] (37.5 kcal/mol was estimated for HF with the same methodology).

In all the afore mentioned studies, it was noticed that the O···H distance between the protons of the hydronium ion (H_3O^+) and the water molecules in the rest of the cluster is about the same for all hydrogen halides, and this was attributed to the fact that the ionic moieties are located at opposite ends of a diamond-like structure (Figure 1), with little effect on the hydrogen bonds. For comparison, in pure water the O···H distance is about

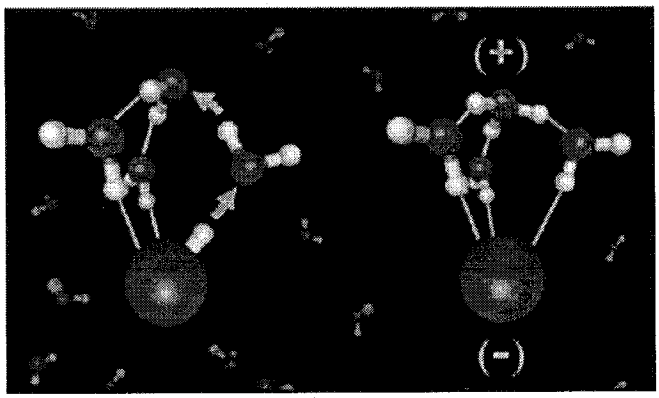

Figure 1. Simplified charge separation process leading to the formation of solvent-separated ion-pair, shown on the right [2].

1.94 Å while in these configurations, the O···H distance is in the range 1.5 – 1.6 Å. Based on geometrical arguments, hydrogen bonding in the diamond-like (ionic) clusters appears stronger, compared to that in pure water clusters of the same size, which may account for the greater stability of the ionic aggregates in comparison to the non-ionized ones. The ability of an acid to dissociate in the presence of a given number of water molecules must

be governed by its acidity [47], and therefore one may expect that HBr will dissociate in smaller clusters than HCl.

The ionization of HBr in small water clusters was specifically explored, simultaneously by two research groups [28, 29]. It was found that HBr also requires four water molecules in order to form an ionic cluster, which as for HCl, appeared to be more stable than the non-ionic species. The cluster was also characterized by a specific diamond-like geometry discussed earlier and free energy calculations [28] suggest that it will remain thermodynamically more stable for temperatures up to 180 K, above which the non-ionic (also known as atop) HBr + $(H_2O)_4$ cluster becomes more stable. As pointed out in the same article, ionization in the presence of three water molecules has not been resolved for HBr, due to subtleties of the calculation. In both studies [28, 29], no ion-pair of three water – acid complex has been found. Despite the propensity of HBr towards dissociation in four-water clusters, in comparison to HCl, the required significant geometrical rearrangements in order to achieve most stable ionic configuration, have led to the conclusion [28] that, like HCl, HBr has to be incorporated into the ice surface.

Along with geometrical parameters and energetics, infrared spectroscopic properties of acid-water clusters help characterize ionization of hydrogen halides in water clusters. For the theoretical prediction to be accurate and reliable, it was shown [42] that infrared frequencies have to be calculated taking into account anharmonic effects and basis set superposition error (BSSE). Excellent correlation with available experimental results was demonstrated when those two factors were accounted for in the case of the one- and two- water clusters of HCl. Alikhani and Silvi [42] have also demonstrated that density-functional methods such as B3LYP (Beck's three-parameter exchange and Lee-

Yang-Parr correlation hybrid functional) have a limited applicability, even when combined with correlation-consistent basis sets, and that coupled cluster theory with single, double and perturbative triple excitations (CCSD(T)) or at least second-order Møller-Plesset perturbation theory (MP2) should be used. Odde et al. [43] have found that the best performance for larger (four- and five-water) clusters is obtained with Møller-Plesset perturbation theory calculations with minimum triple-zeta or 6-311++G** basis sets.

In the last decade, the topological analysis of the electron density known as the Quantum Theory of Atoms in Molecules (QT-AIM) has become a common approach to unambiguously characterize the interatomic interactions in a molecular system. This theory has been successfully applied in many areas of theoretical chemistry for systems as large as enzymes and for transition metals compounds. To date, the only AIM study [49] of the influence of hydrogen halides on the connectivity of a water cluster has been performed on a five-member system, where HX lies atop the pentamer water cluster. This type of acid-water cluster, however, has been previously reported as very unstable and cannot represent a precursor of acid ionization in the presence of water.

I.4. Conclusions

Theoretical investigations of water clusters containing hydrogen halides have a critical role to play in revealing the mechanism of ionization of acids in stratospheric conditions. To date, Møller-Plesset perturbation theory calculations have proven to provide the best estimates of all properties (geometries, energetics, spectroscopic signature, charge distributions, and electron density distributions) necessary in the

characterization of the interatomic interactions and the thermodynamic stability of the molecular clusters. The goals of this thesis are: (a) to provide some insight into ground-state acid ionization in water clusters by characterizing the nature of the bonding interactions in the clusters through an AIM analysis of the electron density; and (b) to characterize the excited states involved in the photoionization of HBr, especially in the presence of water. With these findings, we hope to facilitate future experimental investigations of the spectroscopy, photochemistry and theory of the ionization of hydrogen halides in the presence of water, and to further our understanding of their implication in particular in atmospheric chemistry.

Chapter II.

Bonding Structure and Infrared Spectra of Hydrogen Halide Aqueous Clusters

To be submitted as:

Sacha Z. Zlatkova and Gilles H. Peslherbe, *Journal of Physical Chemistry A*, (2007)

Abstract

The nature of the bonding interactions in water clusters of different size containing HCl or HBr has been investigated by means of electronic structure calculations with second-order Møller-Plesset perturbation theory (MP2), and coupled cluster theory with single, double and perturbative triple excitations [CCSD(T)], combined with a quantum theory of atoms in molecules (AIM) analysis of the electron density. This work shows unambiguously that both HCl and HBr are ionized at cluster size four, though (high-energy) ionized structures of HBr also exist for smaller cluster sizes. Total and Gibbs free energies of formation are also reported at a temperature typical for atmospheric conditions (180K), in order to compare our results with those of previous studies. Further, the infrared spectra of the $HX(H_2O)_n$ clusters, and the shifts of the frequencies relative to those of the gas-phase species in particular, could be rationalized by the bonding structure inferred from AIM analysis.

II.1. Introduction

Ionization of simple acids such as hydrogen halides has long been a key concept in acid-base chemistry and is often implicated in biochemistry [50, 51] and atmospheric chemistry [52]. For instance, there is mounting experimental evidence that the increased production of Cl_2 and Br_2 in the atmosphere is due to the reaction

$$HX + XONO_2 \rightarrow X_2 + HNO_3$$

(where X = Cl and Br), which could first require ionization of hydrogen halides at the liquid ice surface of polar stratospheric cloud particles [41, 53, 54]. However, uncertainties in the reported experimental acid-water interaction energies prevent a firm conclusion on whether the acid is ionized [55, 56] or remains in a molecular form [57] at the surface of liquids. Although a subject of many theoretical studies [18, 19, 28, 29, 35, 36, 40, 43-45, 49, 54], the question of how many water molecules are necessary to ionize a strong acid is still not fully answered [28, 34].

The minimum-energy structures of both HCl and HBr in clusters of up to six water molecules have been relatively well characterized by electronic structure calculations [28, 39, 40, 42-45, 47, 48]. However, to date, with the exception of one study of a five-water cluster [49], all theoretical studies draw conclusions about HCl and HBr ionization on the basis of cluster geometries and vibrational frequencies [42, 58]. It was also shown for $HCl(H_2O)_{1,2}$ clusters that the prediction of proper vibrational spectra requires the inclusion of anharmonicity [42].

Surprisingly, the nature of the bonding interactions in $HX(H_2O)_n$ clusters, which is essential to discriminate between ionized and non-ionized structures, has not been fully

addressed to date. The quantum theory of atoms in molecules (QT-AIM or just AIM) of Bader [59, 60] offers a rigorous approach to characterize bonding interactions in molecules. The applicability of this theory has already been demonstrated for a large number of compounds and molecular complexes such as carbohydrates, peptides, amino acids, transition metal complexes, and hydrogen bonded systems [61]. This theory is thus highly suited to unambiguously characterize ionic, covalent and hydrogen bonds in $HX(H_2O)_n$ clusters. As mentioned earlier, only one study [49] addressed acid ionization not on the sole basis of geometries and spectra, but also on the basis of the nature of bonding interactions inferred from AIM analysis, for a rather unstable [43] five-water cluster, containing HBr and HCl. The characterization of acid ionization from the perspective of bonding interactions in clusters thus requires a more thorough treatment.

The outline of this chapter is as follows. The computational methodology employed in this work is first presented in Section II. The results of our calculations (molecular structures, relative energies, vibrational frequencies and spectra, charge distributions and electron density analysis) are then presented for $HX(H_2O)_n$ (n = 1 - 4) in Section III. A summary and conclusions follow in Section IV.

II.2. Computational Method

Molecular geometries were optimized with second-order Møller-Plesset perturbation theory (MP2) [62-64], and energies were calculated for these geometries with coupled cluster theory with single, double and perturbative triple excitations [CCSD(T)] for clusters containing an acid and up to four water molecules. The augmented correlation-consistent basis set aug-cc-pVTZ [65, 66] was used for H, O and

Cl, while the small core pseudo-potential and augmented correlation-consistent basis set SDB-aug-cc-pVTZ [67, 68] was used for Br. The dissociation energy and the Gibbs free energy of formation of the clusters were calculated according to the formula

$$D_0 = E^{CCSD(T)}{}_{el}\,(HX(H_2O)_n) - E^{CCSD(T)}{}_{el}\,(HX) - nE^{CCSD(T)}{}_{el}\,(H_2O)$$

$$\Delta G^{CCSD(T)} = E^{CCSD(T)}{}_{el} + (\Delta G^{MP2} - E^{MP2}{}_{el}),$$

where $E^{CCSD(T)}{}_{el}$ and $E^{MP2}{}_{el}$ are the total energies calculated at MP2 and CCSD(T) levels of theory, respectively, while the ΔG^{MP2} is the Gibbs free energy of formation calculated for the clusters at MP2 level of theory with a thermal correction at 180K. A vibrational frequency analysis was performed in order to characterize the nature of stationary points, and calculated frequencies were scaled by the standard factor of 0.9546 [28]. Because anharmonicity has been proven significant for these clusters [42, 69, 70], anharmonic frequencies were also calculated by numerical differentiation (second-order perturbative treatment) along the normal modes as implemented in Gaussian03 [71-73]. Energies were corrected for basis set superposition error (BSSE) using the counterpoise method [74, 75] and thermodynamic properties were calculated within the harmonic oscillator-rigid rotor approximation. All calculations were performed with the Gaussian03 suite of programs [73]. The AIM analyses of the electron density and its Laplacian were performed with the AIMPAC suite of programs [76].

The quantum theory of atoms in molecules (AIM) [59] provides means of mapping the topological properties of the electronic density $\rho(r)$ to a Lewis-structure representation of molecules. The theory has been discussed in detail elsewhere [60, 77] and only the key features, relevant for the present study, are reviewed here. A gradient vector field analysis partitions the molecular electronic density into regions or 'basins',

each belonging to a specific atom, and physical properties of atoms can be obtained by integration over the basins. Bond critical points (BCPs) and ring critical points (RCPs) correspond to saddle points of $\rho(r)$, while bond paths are lines of maximum electronic density between two bonded nuclei. The set of bond paths in a molecule defines its molecular graph. The Laplacian of the electronic density $\nabla^2\rho(r)$ identifies regions of local charge concentrations ($\nabla^2\rho(r) < 0$) and local charge depletion ($\nabla^2\rho(r) > 0$) in the topology of the electronic density. The nature of bonding between atoms can be characterized by the value of the electronic density $\rho(r)$ and the sign of the Laplacian of the electronic density $\nabla^2\rho(r)$ at BCPs. A large $\rho(r)$ value together with a large negative $\nabla^2\rho(r)$ value are indicative of sharing of electronic density between atoms, and thus of a shared interaction characteristic of covalent bonding. A low $\rho(r)$ value along with a positive $\nabla^2\rho(r)$ value indicate that the electronic density accumulates in separate atomic basins away from the BCP, a feature representative of a closed-shell interaction typically found in ionic and hydrogen bonding.

II.3. Results and Discussion

The relative stability of $HX(H_2O)_n$ clusters has already been investigated and reported in detail, as described in Section I. Therefore, for the purpose of the present study, we only focus our attention on the most stable configurations. When discussing these structures throughout this chapter, a water hydrogen atom is labeled H_w and the acid hydrogen atom labeled H_a. Free energies of formation and thermodynamical stability have been discussed elsewhere at MP2/aug-cc-pVDZ level of theory [28, 43, 44] and our CCSD(T) data are listed in Table 1. It was already reported that the $X^-H_3O^+$ ion pair is

formed in clusters of size 4 and that it remains thermodynamically stable for low temperatures up to 180K [28]. This temperature is characteristic of atmospheric conditions, therefore Gibbs free energy of formation of all clusters are calculated at this temperature and at CCSD(T) with thermal correction calculated at MP2 levels of theory. The molecular structures and graphs of the most stable $HX(H_2O)_n$ clusters are shown in Figure 2 while contour plots of the Laplacian of the electron density are shown in Figures 3, 5, and 7 – 9.

Table 1. Dissociation and free energies of $HX(H_2O)_n$ (n = 0 – 4) [a]

name	D_e	D_0	ΔG_{180K}
H_2O	0	0	-
HCl	0	0	-
$HCl(H_2O)$	6.0	4.0	0.9
$HCl(H_2O)_2$	14.8	10.0	2.3
$HCl(H_2O)_3S$	25.9	18.3	5.8
$HCl(H_2O)_3D$	21.8	15.2	3.0
$HCl(H_2O)_4D$	37.8	25.2	6.8
$HCl(H_2O)_4C$	38.8	24.4	6.5
$HCl(H_2O)_4P$	35.8	24.2	8.3
HBr	0	0	-
$HBr(H_2O)$	5.1	3.2	0.1
$HBr(H_2O)_2$	13.6	9.0	1.3
$HBr(H_2O)_3S$	24.5	17.2	4.6
$HBr(H_2O)_3D$	22.5	13.3	0.2
$HBr(H_2O)_4D$	40.7	28.0	9.5
$HBr(H_2O)_4C$	38.7	26.3	8.4
$HBr(H_2O)_4P$	33.7	24.1	7.2
$HBr(H_2O)_4$	35.2	25.0	7.9

[a] D_e is the classical dissociation energy, D_0 the zero-point corrected energy and ΔG is the Gibbs free energy (at 180 K), calculated with CCSD(T)/aug-cc-pVTZ. S, C, D, and P identify the square, cyclic, diamond-like, and pentamer structures, respectively (see Figure 2). All energies in kcal/mol.

I.3.a. ***HCl and HBr***. The calculated bond lengths of HCl and HBr are 1.275 Å and 1.409 Å, respectively, which coincide with experimental values (Table 2) [78]. The calculated vibrational frequencies 2981 cm^{-1} for HCl and 2659 cm^{-1} for HBr, are in very good agreement with the experimental values of 2891 and 2649 cm^{-1}, respectively (Table 2 and Figure 3). For both HCl and HBr, not surprisingly, the electronic density ρ at the BCP has large values (Table 2) and the Laplacian $\nabla^2\rho$ is largely negative, which implies a strong covalent interaction. This is further reflected in the contour plots of the Laplacian, in Figure 3, which show a characteristic shared-shell interaction between the hydrogen atom and the halide for both acids. These AIM features for HCl and HBr are used throughout this work to characterize the molecular form of the acid and predict the onset of ionization.

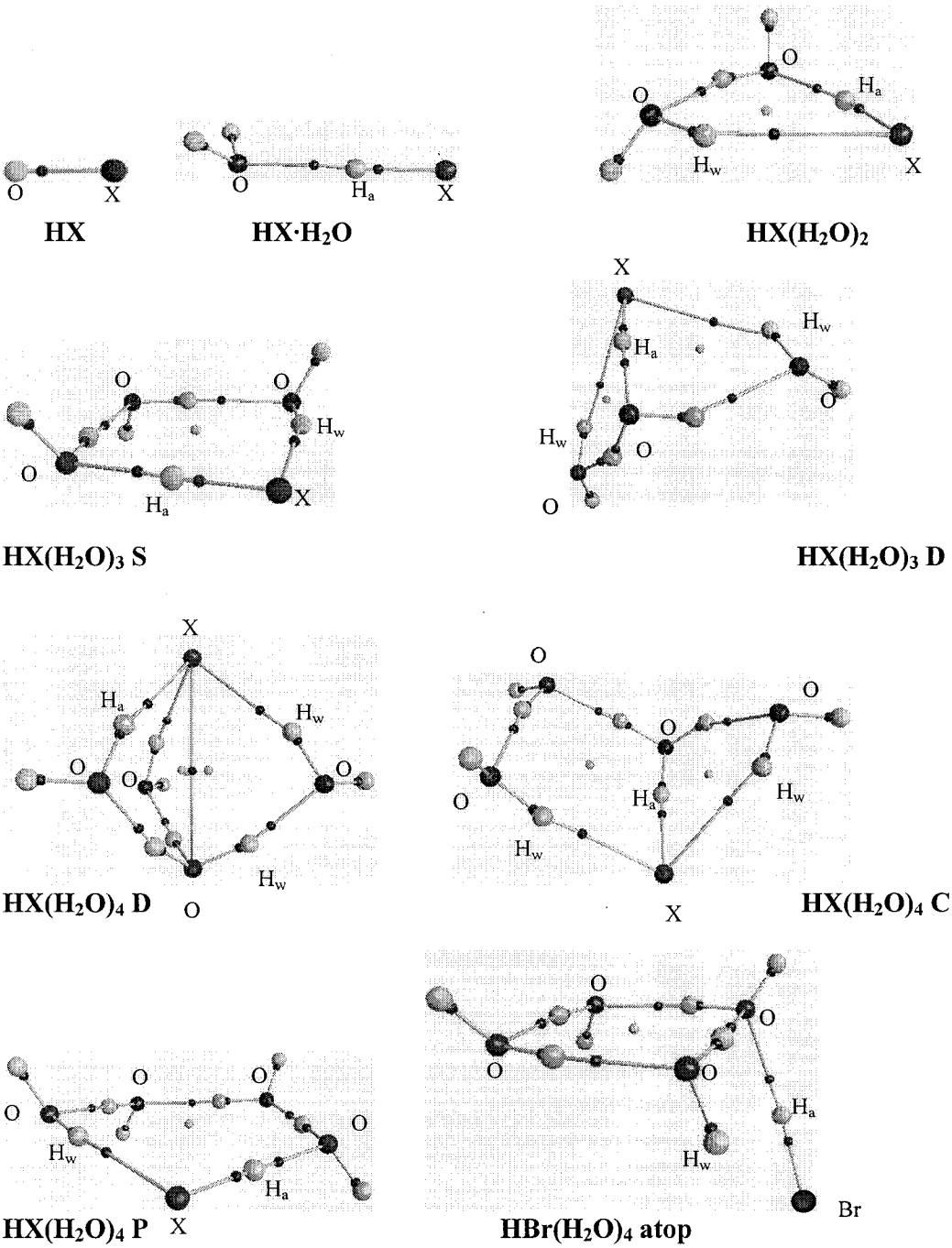

Figure 2. Molecular cluster structures and graphs of $HX(H_2O)_n$ (X=Cl, Br and n = 0 – 4). Small dots along BPs represent BCPs; small dots outside BPs represent ring critical points.

Table 2. Geometrical, electronic and IR-spectroscopic properties of $HX(H_2O)_n$ (n=0-2) [a,b]

		r	$\rho_{BCP}(r)$	$\nabla^2\rho_{BCP}(r)$	$\nu_{(H-X)}$	Exp.[b] $\nu_{(H-X)}(\Delta\nu_{(H-X)})$
H_2O	r_{O-H}	0.961[b]	0.352	-2.04	3631	3657
		-	-	-	3759	3756
					1587	1595
HCl	r_{H-Cl}	1.275[b]	0.251	-0.77	2981	2886
$HCl{\cdot}H_2O$	H_a-Cl	1.289	0.230	-0.86	2748 (138)	2723 (162)
	H_a...O	1.882	0.031	0.10	-	-
$HCl(H_2O)_2$	H_a-Cl	1.328	0.218	-0.81	2412 (474)	2464 (422)
	H_a...O	1.718	0.044	0.13	-	-
	H_w...Cl	2.604	0.011	0.03	-	-
HBr	r_{H-Br}	1.409[b]	0.199	-0.41	2659	2649
$HBr{\cdot}H_2O$	H_a-Br	1.432	0.192	-0.42	2463 (186)	2446 (203)
	H_a...O	1.936	0.028	0.08	-	-
$HBr(H_2O)_2$	H_a-Br	1.462	0.184	-0.43	2171 (478)	2328 (321)
	H_a...O	1.742	0.043	0.12	-	-
	H_w...Br	2.725	0.010	0.02	-	-

a. Distances in Å, angles in degrees, ρ in e/Å^3, and $\nabla^2\rho$ in e/Å^5. H_a refers to the acid hydrogen, H_w the water hydrogen. Only the shortest H_a...O value is reported. Anharmonic ν(H-X) frequencies in cm^{-1}.Values in parenthesis indicate red-shift of the H-X frequency with respect to gas-phase. All results are calculated with MP2/aug-cc-pVTZ.

b. Experimental results: r_{O-H}=0.958 Å, <H-O-H=104.5 degrees, r_{H-Cl}= 1.275 Å and r_{H-Br}=1.409 Å are taken from reference [78], $\nu_{(H-X)}(\Delta\nu_{(H-X)})$ are taken from reference [42].

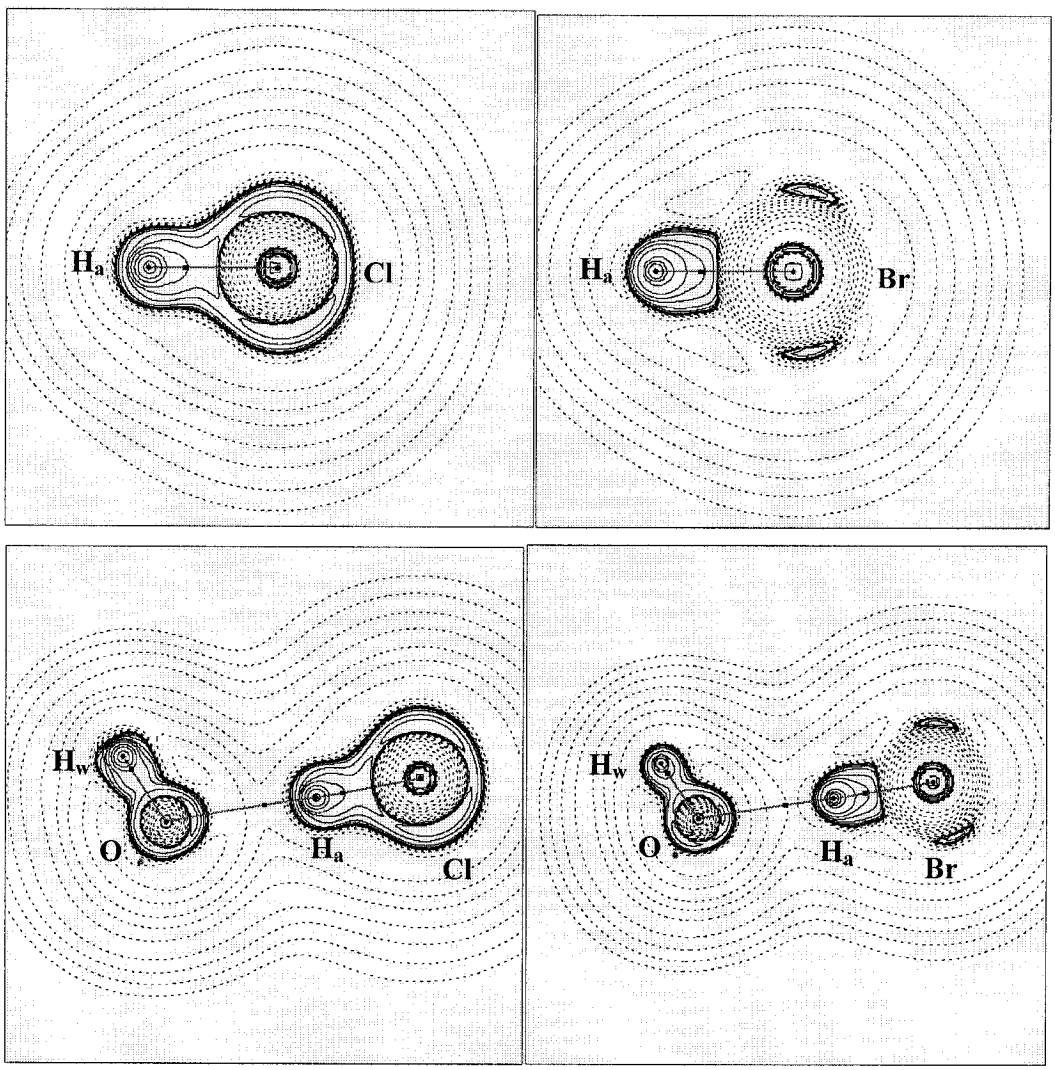

Figure 3. Contour plots of the Laplacian of the electronic density $\nabla^2\rho$ for HX and $HX(H_2O)$, in the $X–H_a\cdots O\cdots H_w$ plane. Dashed lines correspond to positive $\nabla^2\rho$ (regions of electronic charge depletion), solid lines to negative $\nabla^2\rho$ (regions of electronic charge concentration); Bond paths are denoted by solid straight lines and BCPs by solid squares, atoms outside the indicated plane appear as dots.

II.3.b. ***$HX(H_2O)$ and $HX(H_2O)_2$*** The complexes of HX with one water molecule have been well characterized in terms of geometries and energetics [39, 43, 44]. The H-X bond distances are slightly elongated, by 0.014 Å and 0.023 Å, and the corresponding stretching

vibrational frequencies red-shifted by 234 cm^{-1} and 189 cm^{-1} for Cl and Br, respectively (Table 2). The trend of bond elongation for H-X is retained in the two-water clusters, where the HX bond is larger by 0.053 Å for both Cl and Br, compared to the gas-phase H-X bond. The H-X vibrational frequencies in $HX(H_2O)_2$ are further red-shifted, by 477 cm^{-1} and 441 cm^{-1} for Cl and Br, respectively. The internuclear interactions in the water molecules are less affected by the presence of the hydrogen halide for the one-water complex as well as the two-water clusters. The electronic density at the BCPs of H_w-O is 0.35 e/Å^3 and the Laplacian is –2.08 e/Å^5 for water, and these values are practically unchanged in the complexes (Table 2). The contour plot of the Laplacian in Figure 3 supports this trend: the H_w-O interaction is shared-shell for $HX(H_2O)$ as well as for $HX(H_2O)_2$ (not shown). The infrared spectra for these clusters, shown in Figure 4, contain insignificant changes (20 – 30 cm^{-1}) in the frequencies of the water modes with respect to gas-phase water. While the atomic charge (Table 3) on Cl and H_a does not change (-0.22 and 0.22), it almost doubles for Br and O (-0.22 and -0.63), respectively, in comparison to gas-phase molecules, indicating that the dipole-dipole interaction for HBr-water is stronger than that for HCl-water in both $HX(H_2O)$ and $HX(H_2O)_2$. The hydrogen-halide bonding interaction is covalent for both cluster sizes, according to the characteristic shared-shell interaction evident from the contour plot of the Laplacian (Figure 3, the contour plots for $HX(H_2O)_2$ are not shown but are similar). The values of ρ_{BCP} and $\nabla^2\rho_{BCP}$ for the H_a-X BCPs are slightly changed (0.23 to 0.21 e/Å^3 and –0.85 to –0.80 e/Å^5, 0.192 to 0.184 e/Å^3 and –0.42 to –0.43 e/Å^5 for Cl and Br, respectively) in comparison to gas-phase, indicating that the covalent interaction of the hydrogen halide is retained in one and two water complex, however, the

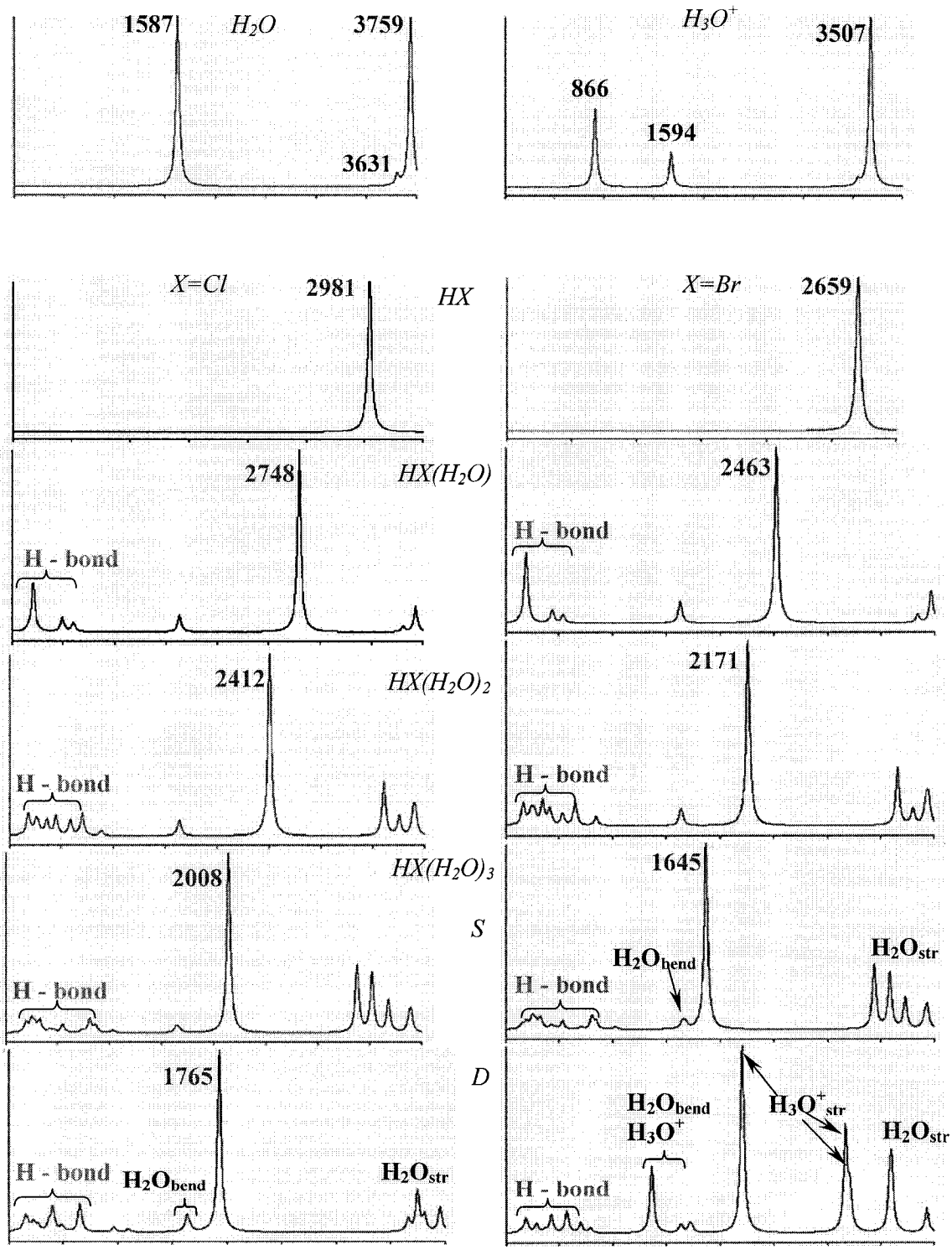

Figure 4. Calculated infrared spectra of H_2O, H_3O^+, and $HX(H_2O)_n$, n = 0-3.

Table 3. Atomic charges for $HX(H_2O)_n$ (n = 0 – 4) [a]

name	X	H_a	H_w	O
H_2O	-	-	0.16	-0.31
HCl	-0.22	0.22	-	-
$HCl{\cdot}H_2O$	-0.25	0.17	0.34	-0.60
$HCl(H_2O)_2$	-0.27	0.22	0.30	-0.67
$HCl(H_2O)_3S$	-0.30	0.23	0.31	-0.68
$HCl(H_2O)_3D$	-0.32	0.23	0.31	-0.71
$HCl(H_2O)_4D$	-0.71	0.32	0.54	-0.64
$HCl(H_2O)_4C$	-0.84	0.66	0.38	-0.60
$HCl(H_2O)_4P$	-0.33	0.24	0.34	-0.70
HBr	-0.16	0.16	-	-
$HBr{\cdot}H_2O$	-0.21	0.14	0.35	-0.63
$HBr(H_2O)_2$	-0.22	0.17	0.28	-0.67
$HBr(H_2O)_3S$	-0.26	0.18	0.28	-0.67
$HBr(H_2O)_3D$	-0.54	0.27	0.25	-0.52
$HBr(H_2O)_4D$	-0.57	0.42	0.25	-0.65
$HBr(H_2O)_4C$	-0.55	0.39	0.26	-0.61
$HBr(H_2O)_4P$	-0.28	0.16	0.29	-0.72
$HBr(H_2O)_4$	-0.15	-0.04	0.32	-0.43

[a] In fraction of e. Calculated from AIM analysis of the MP2/aug-cc-pVTZ wavefunction. The C, D, and P labels refer to the cyclic, diamond-like and pentamer structures. H_w is the water hydrogen closest to the halide atom or the hydronium ion hydrogen for $HX(H_2O)_{3,4}$ S, C and D. The oxygen charges are those of the donor oxygen for $HX(H_2O)_4$ P and the hydronium ion oxygen for $HX(H_2O)_{3,4}$ S, C and D.

increasingly red-shifted H-X stretching vibrational frequencies suggest increasing weakening of the acid bond with cluster size, while the water is not significantly affected by the acid for these two clusters.

II.3.c. ***$HX(H_2O)_3$*** The two most stable configurations of three-water clusters (Figure 2), exhibit a square configuration, referred to as $HX(H_2O)_3$ S [43, 44] and a "diamond-like" configuration, referred to as $HX(H_2O)_3$ D [28, 43, 44]. The square conformation is energetically more stable than the diamond-like one by 3.1 kcal/mol and 3.9 kcal/mol for

HCl and HBr, respectively, in good agreement with previous works [28, 29, 43, 44]. From the data for the Gibbs free energy of formation (Table 1) one can see, that even though the S clusters are more stable, their formation is less preferable than the D clusters, which is in qualitatively good agreement with previous results [43]. In $HX(H_2O)_3$ S the acid bond distance H_a–X is 1.33 Å and 1.49 Å for Cl and Br, but still smaller than the shortest halide-water hydrogen bond distance X···H_w (above 2.3 Å) for both acids. Contrary to this in $HX(H_2O)_3$ D, the H_a–X bond distance is further elongated

Table 4. Geometrical, electronic and IR-spectroscopic properties of $HX(H_2O)_3$[a]

		r	$\rho_{BCP}(r)$	$\nabla^2\rho_{BCP}(r)$	$\nu_{(H-X)}$
$HCl(H_2O)_3$ S	H_a-Cl	1.330	0.203	-0.73	2008 (982)
	H_a...O	1.626	0.060	0.14	
	H_w...Cl	2.319	0.017	0.05	
$HCl(H_2O)_3$ D	H_a-Cl	1.388	0.198	-0.52	1765 (1216)
	H_a...O	1.491	0.080	0.10	
	H_w...Cl	2.629	0.010	0.03	
$HBr(H_2O)_3$ S	H_a-Br	1.487	0.161	-0.33	1645 (1003)
	H_a...O	1.596	0.064	0.14	
	H_w...Br	2.469	0.016	0.04	
$Br^-(H_2O)_2H_3O^+$ D	H_a-Br	1.942	0.057	0.05	-
	H_a...O	1.066	0.248	-1.09	
	H_w...Br	2.460	0.017	0.04	

[a] Distances in Å, ρ in e/Å^3 and $\nabla^2\rho$ in e/Å^5. Results are calculated with MP2/aug-cc-pVTZ. Anharmonic ν(H-X) frequencies in cm^{-1}.Values in parenthesis indicate red-shift of the H-X frequency with respect to gas-phase. H_a refers to the acid hydrogen, H_w the water hydrogen. Only the shortest H_a...O value is reported. S and D refer to the square and diamond-like structures, respectively (see Figure 2).

up to a value of 1.39 Å and 1.94 Å, for Cl and Br, respectively. This change in geometry between the S and D configurations is expressed through different hydrogen bond formation. Thus, for the S clusters, HX is forming hydrogen bonds only with the adjacent two waters,

while in the D clusters the acid is forming hydrogen bond with all three water molecules. The IR spectra (Figure 4 and Table 4) of the square acid-water conformations show distinguished features of acid stretching with frequency of 2008 cm^{-1} and 1645 cm^{-1} for H–Cl and H–Br, respectively. On these spectra, water symmetric stretching is more intense with a red shift of 102 cm^{-1} and 179 cm^{-1} for Cl and Br respectively in comparison to the gas-phase water symmetric mode, than the corresponding asymmetric vibrational modes for both acid-water complexes. Bending water vibrational modes are more blue shifted for Br (by 110 cm^{-1}) than for Cl (85 cm^{-1}) but both features of the water IR spectra indicate deformation of the water cluster due to the presence of acid. The appearance of a single-peak stretching vibration, even more red-shifted than the ones observed for HX, $HX(H_2O)$ and $HX(H_2O)_2$, by 752 cm^{-1} and 805 cm^{-1} for Cl and Br, respectively, compared to the isolated HX is an indication that HX in these cluster configurations is not ionized but weakened. For this bond interaction the electron density in the BCP has values of 0.20 $e/Å^3$ and 0.16 $e/Å^3$, which are lower than the corresponding gas-phase values, while the Laplacian is less negative (-0.73 $e/Å^5$ and -0.33 $e/Å^5$) for Cl and Br, respectively. The acid hydrogen halide internuclear interaction H_a–X is shared-shell on the corresponding contour plots of $\nabla^2\rho$. The latter indicating weakening of the covalent H_a–X interaction in $HX(H_2O)_3$ S.

The corresponding calculated internuclear distances H_a–X are 1.39 Å and 1.94 Å, whereas the shortest O···H_a and X···H_w are 1.49 and 2.63 Å for Cl and 1.07 and 2.46 Å for Br, respectively. This is the first situation in these cluster groups when bonding properties of HBr differ from HCl having the H_a–Br and Br···H_w distances longer than the corresponding O···H_a ones. Further investigation of these properties from the calculated IR spectra (Figure 4) reveal that the H_a–Br stretching vibrational frequency is disappeared instead of the

existing three OH stretches corresponding to a H_3O^+ structure, where the asymmetric as well as the symmetric vibrational frequencies of H_3O^+ are strongly red-shifted, indicating weakly bonded H_3O^+ ion. From the analysis of the electron density in the bond critical points of H_a–Br and H_w···Br has very small values

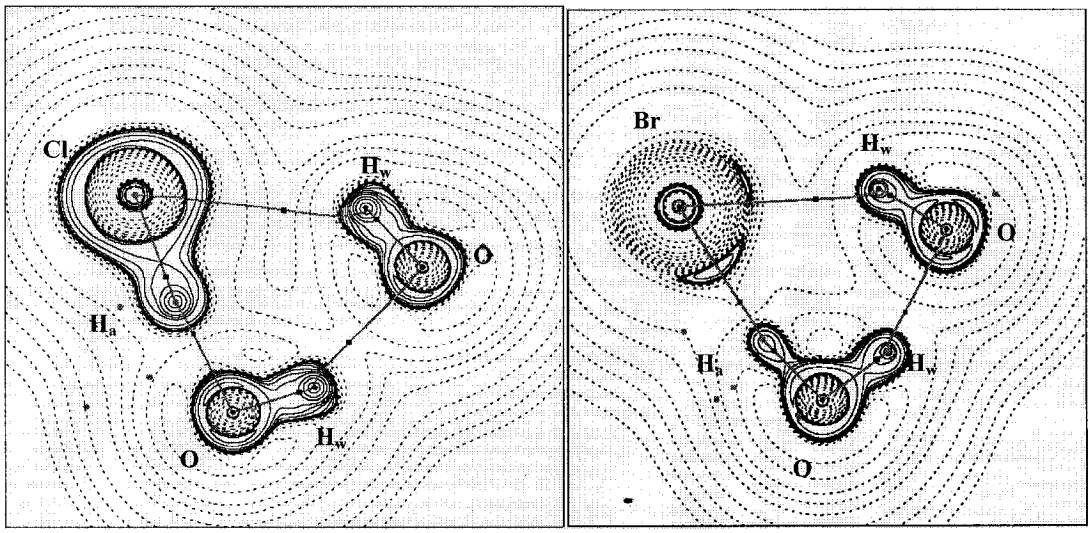

Figure 5. Contour plots of the Laplacian of the electron density for the $HX(H_2O)_3$ D cluster. See Figure 3 for caption details.

0.06 e/Å^3 and 0.02 e/Å^3, while the Laplacian in these BCPs is positive, 0.05 e/Å^5 and 0.04 e/Å^5, respectively constituting ionic interactions as well as closed-shell contour of the Laplacian (Figure 5, right) in contrast to a shared-shell interaction for $HCl(H_2O)_3$ D (Figure 5, left). The atomic charges (Table 3) on the water are equally negative in $HCl(H_2O)_3$ D but in $HBr(H_2O)_3$ D the central oxygen has less negative charge than the outermost members. This indicates that as the negative charge on the central oxygen is withdrawn and more concentrated on Br, hydronium ion formation occurs particularly in $HBr(H_2O)_3$ D cluster. By this contrast between properties of $HX(H_2O)_3$ D and $HX(H_2O)_3$ S, it is evident that for Br

ionized complex occurs at cluster size 3, while in both clusters the water network in strongly affected by the presence of the acid.

II.3.d. ***$HX(H_2O)_4$.*** Contrary to the $HX(H_2O)_3$, the most stable $HX(H_2O)_4$ appear to be diamond-like $HX(H_2O)_4$ D cluster, followed closely by the cyclic (or open-book-like) $HX(H_2O)_4$ C cluster configuration. The $HCl(H_2O)_4$ D cluster is 0.8 kcal/mol and $HBr(H_2O)_4$D is 1.6 kcal/mol more stable than are the cyclic ones (Table 1). For both Cl and Br diamond-like clusters, all shortest H···X distances differ only by 0.02 Å and have values the range 2.25 Å – 2.10 Å, an indication for a very weak hydrogen halide interaction. The vibrational spectra (Figure 5) of the diamond-like cluster structures have grouped O-H stretching modes corresponding to the water molecule vibrational motions followed by O-H stretching of the H_3O^+, a cluster of bending H–O–H for both H_2O and H_3O^+ and at the low-frequency end of the spectrum hydrogen-bonding frequency network. The Laplacian contour plots for both Cl and Br containing clusters evidence a closed-shell interaction for the shortest H···X distances (Figure 7), supporting further HCl and HBr ionic complexation with the water in these configurations. Only in these two clusters C and D the charge on X is most negative while the negative charge on the O corresponding to the hydronium ion much smaller than that of the outermost water oxygen atoms, an indication of ion pair formation. For these two clusters all values of ρ_{BCP} for H_a...O are large, 0.26 e/Å^3 (4C) and 0.33 e/Å^3 (4D) for Cl; 0.29 e/Å^3 (4C) and 0.33 e/Å^3 (4D) for Br, while the corresponding values of the Laplacian in these BCPs are large negative, -1.79 e/Å^5 (4C), -2.48 e/Å^5 (4D) for Cl; -2.02 e/Å^5 (4C), -2.50 e/Å^5 (4D) for Br. This is to show that all short H_a...O, within the range of bond interaction distances, have covalent character.

Table 5. Geometrical, electronic and IR-spectroscopic properties of $HX(H_2O)_4$[a]

		r	$\rho_{BCP}(r)$	$\nabla^2\rho_{BCP}(r)$	$\nu_{(H-X)}$
$Cl^-(H_2O)_2H_3O^+$ C [b]	H_a-Cl	1.779	0.069	0.04024	-
	H_a...O	1.058	0.264	-1.75160	
	H_w...Cl	2.211	0.022	0.06132	
$Cl^-(H_2O)_2H_3O^+$ D [c]	H_a-Cl	-	-	-	-
	H_a...O	0.990	0.328	-2.47607	
	H_w...Cl	2.066	0.035	0.07212	
$HCl(H_2O)_4$ P	H_a-Cl	1.338	0.214	-0.66946	2004.60 (976)
	H_a...O	1.583	0.061	0.12248	
	H_w...Cl	2.271	0.021	0.05812	
$Br^-(H_2O)_2H_3O^+$ C [b]	H_a-Br	2.005	0.051	0.04244	-
	H_a...O	1.034	0.285	-2.02455	
	H_w...Br	2.353	0.025	0.05528	
$Br^-(H_2O)_2H_3O^+$ D [c]	H_a-Br	-	-	-	-
	H_a...O	0.988	0.332	-2.50477	
	H_w...Br	2.238	0.030	0.05767	
$HBr(H_2O)_4$ P	H_a-Br	1.513	0.164	-0.36968	1658.81 (1001)
	H_a...O	1.506	0.076	0.10324	
	H_w...Br	2.409	0.019	0.04892	
$HBr(H_2O)_4$ atop [d]	H_a-Br	1.439	0.194	-0.4612	2365.72 (294)
	H_a...O	4.90	0.032	0.09552	
	H_w...Br	3.275	no BCP	no BCP	

a. Distances in Å, ρ in e/ Å^3 and $\nabla^2\rho$ in e/ Å^5. Results are calculated with MP2/aug-cc-pVTZ. Anharmonic ν(H-X) frequencies in cm^{-1}.Values in parenthesis indicate red-shift of the H-X frequency with respect to gas-phase. H_a refers to the acid hydrogen, H_w the water hydrogen. Unless specified otherwise, only the shortest H_a...O value is reported. C, D, and P refer to the cyclic, diamond-like, and pentamer structures, respectively (see Figure 2).

b. The shortest H_a-X value is given, while the H_a...O value corresponds to the OH distance in the hydronium ion, towards the bromine.

c. For H_a...O the averaged value of all OH distances pointing towards the halide is given, for H_w...Br the averaged value is given.

d. Only the shortest H_w...Br value is given.

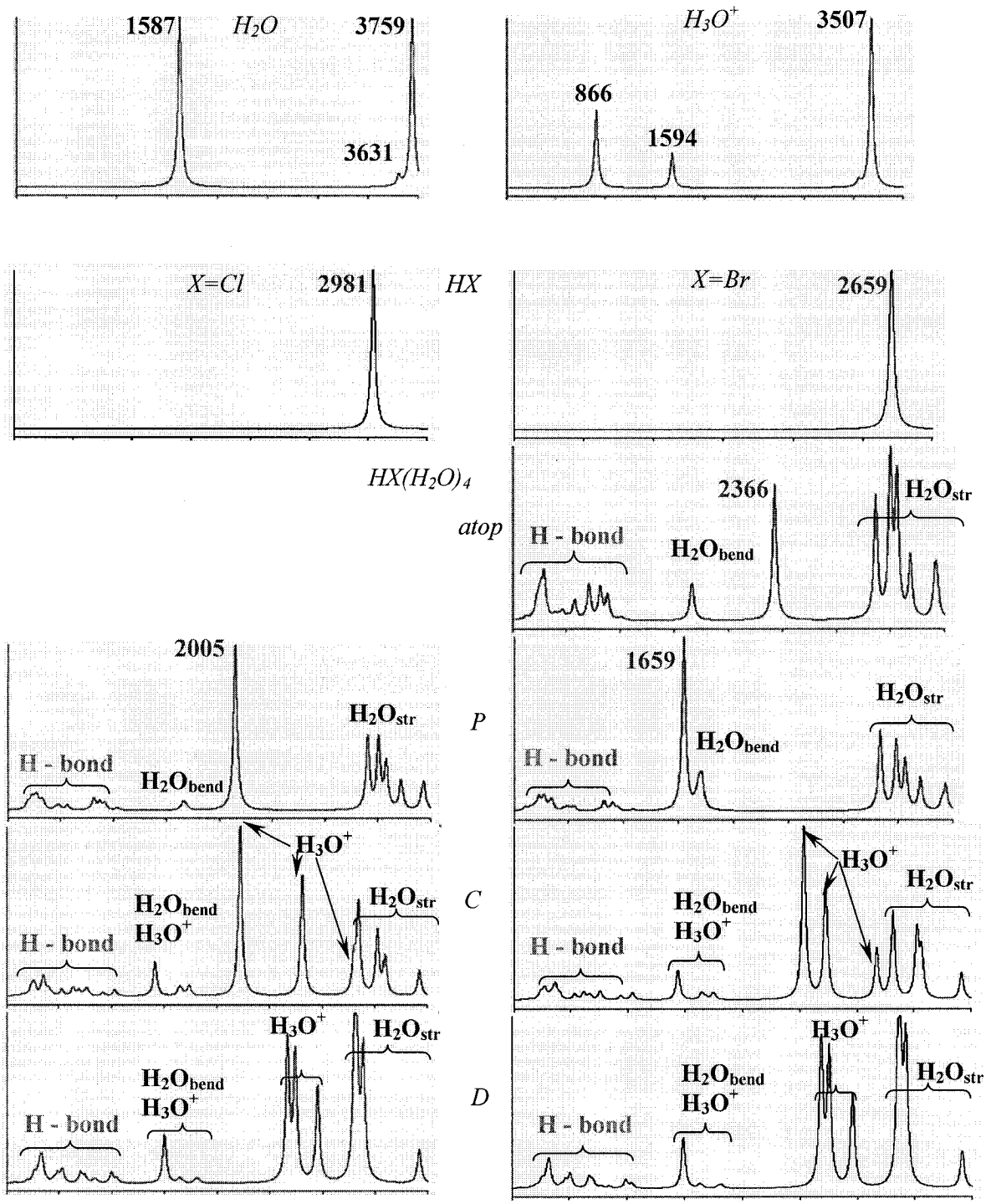

Figure 6. Calculated infrared spectra of H_2O, H_3O^+, HX, and $HX(H_2O)_4$.

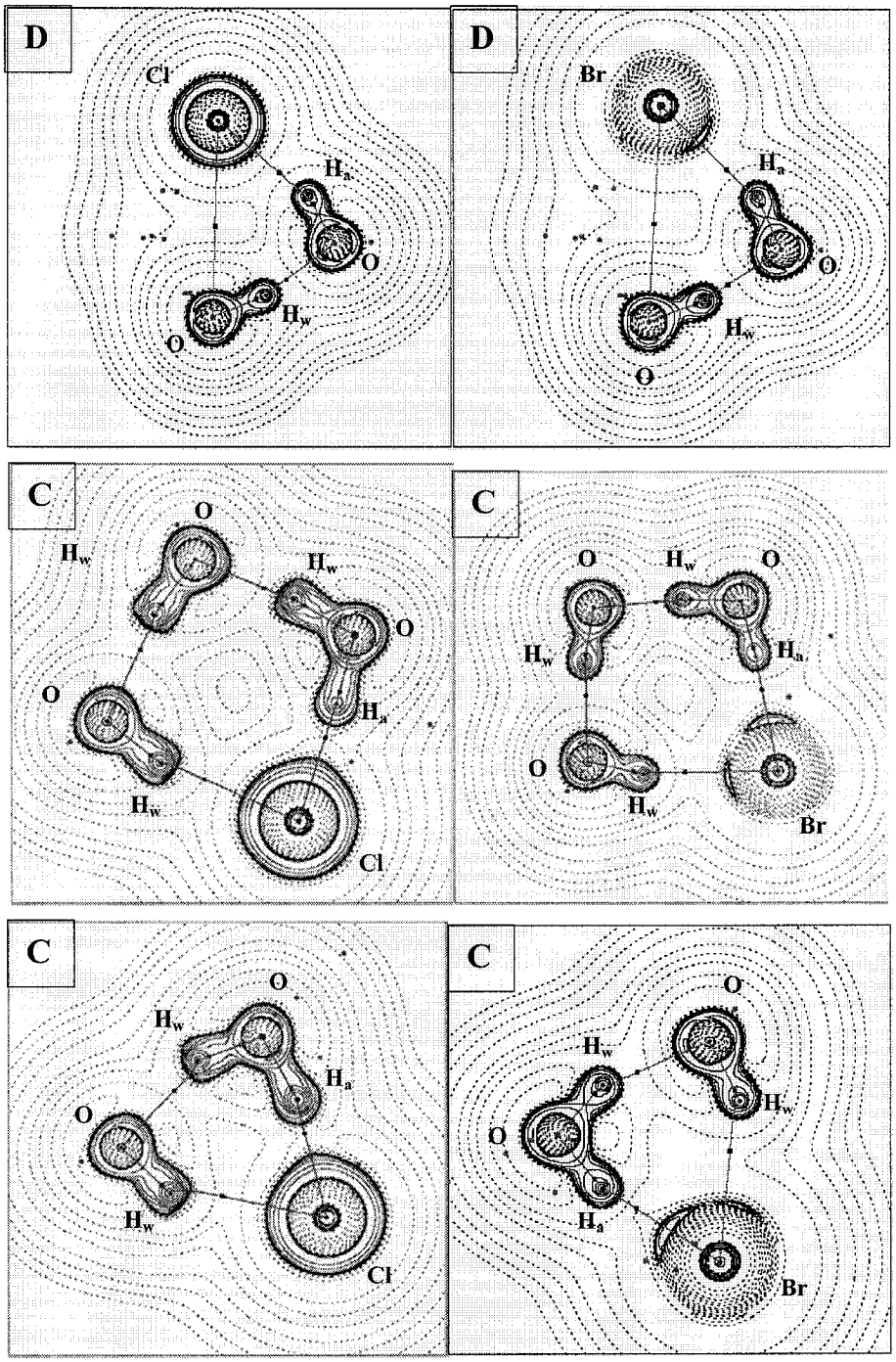

Figure 7. Contour plots of the Laplacian of the electron density for $HX(H_2O)_4$ D and $HX(H_2O)_4$ C clusters. See Figure 3 for caption details.

Contrary to this, for the BCPs at all short H_w...X distances the electron density has very low values: 0.02 e/Å^3 (4C), 0.03 e/Å^3 (4D) for Cl and Br, respectively. The later shows ionic character of the X-H interaction within a bond range. At the same time, large negative values of the atomic charges of -0.71 and -0.57 for Cl and Br, respectively and large positive atomic charges on the closest hydrogen of 0.42 and 0.32, are to show the electronic charge is localized for the D and C clusters on X^- and H from the hydronium ion. Lastly, the existence of a bond path between X and O of the hydronium ion in the 4D clusters of Cl and Br is a result of the strong ion-dipole interaction between these two cluster moieties which is responsible for the energetic stability of this cluster form.

Less stable than the diamond-like $HX(H_2O)_4$ D is an in-plane pentamer $HX(H_2O)_4$ P which is higher in energy by 1.0 kcal/mol for Cl and 3.9 kcal/mol for Br, respectively. This cluster exhibits different features for the two acids. In the case of HCl, a single infrared peak corresponding to the H–Cl stretching mode is separated from the water-bending modes cluster, although red-shifted with respect to the gaseous H–Cl by 860 cm^{-1}. The red shift of the analogous H–Br stretching mode is 1108 cm^{-1} but it occurs at lower frequency than the water-bending modes and it overlaps with them (Figure 6). The corresponding bond distances are elongated from their equilibrium values (HX in a gas phase) by 0.06 Å and 0.10 Å, which suggest that the HBr bond interaction is weakened in the presence of the water molecules for this configuration. The analysis of the charge density and its Laplacian confirm the latter suggestion by the high values of ρ (0.21 and 0.16, for Cl and Br, respectively) at the bond critical points between the H and X nuclei with respect to the values in these points for isolated acids (0.25 and 0.20).

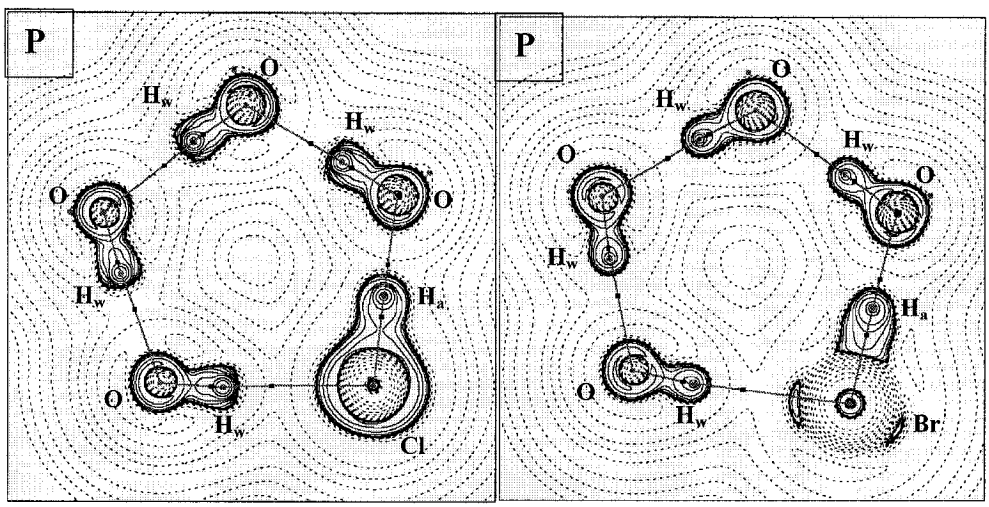

Figure 8. Contour plots of the Laplacian of the electron density for $HX(H_2O)_4$ P cluster. See Figure 3 for caption details.

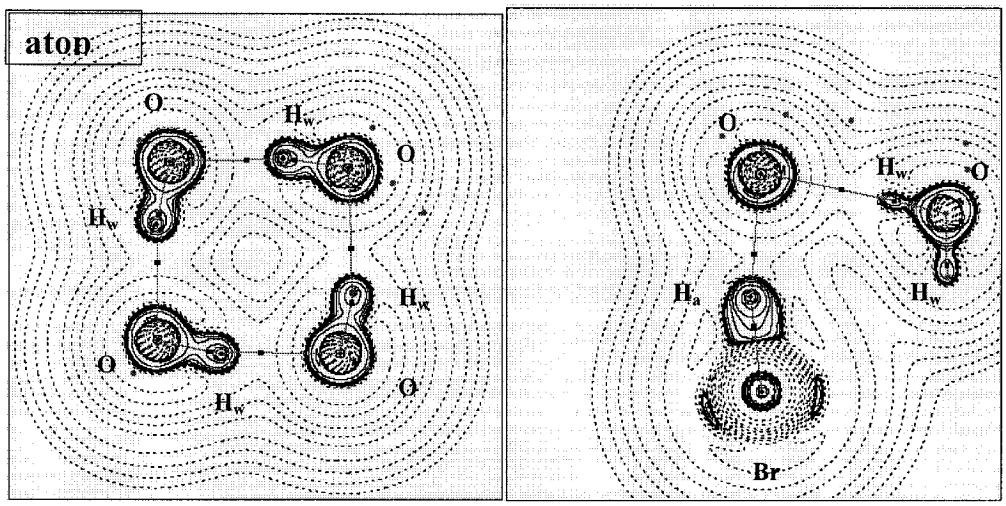

Figure 9. Contour plots of the Laplacian of the electron density for $HBr(H_2O)_4$ atop cluster in two planes. See Figure 3 for caption details.

The Laplacian at the H–X bond critical point are large and negative, suggesting that the HX bonding interactions are strongly covalent (Table 5). The same character is observed for the H–Br interaction in the "atop" cluster configuration, which is less stable than the ionized diamond-like configuration by 2.9 kcal/mol.

From the spectra on Figure 6, despite the large red shift of 976 $cm^{-1}$and 1001 cm^{-1} for Cl and Br, respectively, the H–X stretching in the P conformations, the stretching vibration of water are much more intense and slightly shifted to lower frequency as well. This can be attributed to the weakening of the O–H bonds leading to their instability with respect to the D-clusters. Lastly, in the ionized D and C clusters the H–X modes are completely replaced by the modes characteristic for hydronium ion. This comes to show that the presence of HX also affects the structure of the water cluster and the bond dissociation in the acid is accompanied by more hydrogen bond formation in the entire cluster.

II. 4. Summary and Conclusions

In this chapter, the nature of the bonding interactions in water clusters containing the strong acids HCl and HBr has been investigated in terms of geometries, the topology of the electron density distribution and vibrational spectra. The results show that HBr ionizes in a smaller water cluster than HCl, even though the ionized complex is less stable than the non-ionized one. One of the most important findings is that ionization of HCl and HBr occurs while a step-wise hydrogen halide bond weakening (with cluster size) correlates with an increasing red shift of the corresponding H-X vibrational frequency, blue shift of the water bending frequencies and disappearance of the acid stretching frequency mode.

These features are supported by the AIM analysis of the $HX(H_2O)_n$ (n = 0 – 4) electron density distribution. The covalent H-X bond is increasingly weakened as a function of cluster size up to cluster size 4. The values of ρ_{BCP} in BCP for the H-X bond in all 0 to 3 clusters sizes gradually decreases from maximum values of 0.25 $e/Å^3$ and 0.19 $e/Å^3$ in the gas-phase HX to minimum values of 0.19 $e/Å^3$ and 0.16 $e/Å^3$ in the 3S clusters for Cl and Br,

respectively. For the BCPs of HX in these nonionized clusters, the Laplacian $\nabla^2\rho_{BCP}$ changes from, -0.77 e/Å^5 and -0.42 e/Å^5 to -0.52 e/Å^5 and -0.33 e/Å^5 in 3-S clusters for Cl and Br, respectively. This decrease in values of the electronic density and the Laplacian, as introduced in the beginning, are evident for weakening of the hydrogen halide bond. Sudden change of 0.06 e/Å^3 and 0.05 e/Å^3 for ρ_{BCP} and 0.04 e/Å^5 for $\nabla^2\rho_{BCP}$ occurs in the H···X BCPs of the 4C cluster, where the HX interaction becomes ionic for the ionized $X^-(H_2O)_3H_3O^+$ clusters, where the electronic density and the Laplacian exhibit low and positive values, respectively, characteristic for ionic interaction. We also demonstrated that while in the nonionized clusters the H_a-X frequency is gradually and strongly red-shifted with respect to the gas-phase spectra of HX, such frequency disappears from the spectra of the ionized 4D and 4C clusters. Finally we hope that this study provides additional insight in the mechanism of ionization of HCl and HBr in the presence of water in support to previous works [28] when ionization of HBr in small water clusters was discussed in the light of different temperature regimes and postulated to occur in cluster size 4 for the first time.

Chapter III.

A High-Level Quantum Chemistry Characterization of HBr Photoionization

To be submitted as:

Sacha Z. Zlatkova and Gilles H. Peslherbe, *Journal of Chemical Physics*, (2007)

Abstract

The excited and Rydberg states of HBr were investigated with multireference configuration interaction (MRCI) calculations with the aug-cc-pVTZ basis set. Particular attention was paid to the first Rydberg $C^1\Pi$ state, the intermediate $E^1\Sigma$ and the ion-pair $V^1\Sigma$ states for their relevance to HBr photoionization. Results show that spin-orbit coupling plays an important role in the relative position of the potential energy curves due to mixing of the ion-pair and Rydberg states. The spectroscopic properties calculated for the first, third and fifth vibrational level of the ion-pair and Rydberg $E^1\Sigma$ states are in a good agreement with previously reported values. The potential energy curves of the Rydberg $C^1\Pi$, the intermediate $E^1\Sigma^+$, the ion-pair state $V^1\Sigma^+$ and their triplet counterparts $b^3\Pi$, $e^3\Sigma^+$ and $t^3\Sigma^+$ are fully characterized for the first time in terms of Franck-Condon vertical excitation energies. The first four vibrational levels of the Rydberg $C^1\Pi$ state were also calculated in order to explain the uneven distribution of the vibrational levels in the other two $V^1\Sigma$ and $E^1\Sigma$ states, which are known to all interact via spin-orbit coupling. A possible rationalization of the mechanism of HBr photoionization was given based on these results.

III.1. Introduction

Studies of diatomic molecules such as hydrogen halides HX (X = Cl, Br, and I) are important due to spin-orbit coupling effects [79, 80] resulting in large perturbations of the molecular rovibrational spectra and potential energy surfaces [81]. Among all hydrogen halides, HCl has receiving significant attention from the experimental and theoretical standpoint, mostly due to the relatively small size of the chlorine atom (compared to bromine and iodine), which results in a simpler spectrum for the valence and excited states. More specifically, the potential energy curves and transition dipole moments of HCl have been investigated theoretically in great detail [82, 83], providing a reference for further analogous studies of the other members of the HX series. The interest in the excited states of HBr stems from theoretical and spectroscopic characterization of the intermediate HBr Rydberg region and the implications of those properties for atmospheric processes related to ionization. Relativistic effects, resulting from the large size of the bromine atom, also complicate the electronic structure of the HBr excited states. Despite the large amount of experimental data on rovibrational constants, energetics, transition moments, and vibrational spectra around the HBr equilibrium internuclear distance, characterization of those properties for the ion-pair state and the states that can interact with it is still largely incomplete.

Stamper and Barrow reported for the first time lines in the absorption spectrum of HBr in the range 66,700 to 85,700 cm^{-1}, but no precise assignment of the states involved in the transitions was given [84, 85]. Later, Baig and co-workers made assignments on the basis of measured synchrotron radiation spectra [86], but the most detailed assignment of the bands of HBr below 79,500 cm^{-1} to date has been reported by Ginter et al. [87]. Ascenzi et al. [88] employed resonance-enhanced multiphoton ionization spectroscopy with time-of-flight

resolution to measure and characterize the lines in the $H^{81}Br$ spectrum in the absorption region 81,900 – 94,900 cm^{-1}. A total of 34 bands were analyzed and assigned to transitions from the ground $X^1\Sigma^+_{0+}$ state of HBr to Rydberg states from the (6,7,8)sσ, (6,7,8)pσ, 4dπ, 6pπ, 4dδ, and (5,6) dδ manifolds, and to the second and third vibrational levels of the $E^1\Sigma^+$ state. This work, along with previous theoretical [89, 90] and experimental [85] investigations of the higher vibrational levels of the intermediate $E^1\Sigma^+$ and ion-pair $V^1\Sigma^+$ valence states, allowed to draw the following conclusions: (a) the valence state has a strong perturbation effect on the vicinal $^1\Sigma^+_{0+}$ and $^3\Sigma^-_{0+}$ states, and in particular on the $E^1\Sigma^+$ state; (b) the result of this strong interaction is a compression of the rovibrational levels of the E-manifold and an expansion of the levels in the V-state near the equilibrium distance; (c) such perturbations caused by the V-state were found to even affect the Δ states, as $F^1\Delta - V^1\Sigma^+$ near-resonant interactions were detected for both HCl and HBr [90].

Detailed theoretical investigations of the $(\sigma^2\ \pi^3)\ \sigma^*$ manifold ($A^1\Pi$ and $a^1\Pi_i$, i = 0,1,2) were reported by Péoux and co-workers [91], who simulated the dynamics of HBr photofragmentation by means of time-dependent, time-independent and semiclassical methods. A similar study was very recently reported by Smolin et al. [92]. Both studies indicated that spin-orbit branching at larger photon wavelengths is governed by the initial excitation to both the $A^1\Pi$ and $a^3\Pi$ (Ω=0) states, a conclusion that was drawn on the basis of potential energy curves, transition moments, and spin-orbit coupling matrix elements. A theoretical analysis of twelve electronic states including singlet, doublet and triplet states up to high Rydberg energies was performed by Chapman and co-workers [84], in a study which is the most detailed investigation to date of the HBr electronic spectra. They reported vertical Franck-Condon energies of 71,154 cm^{-1} and 74,889 cm^{-1} for the $b^3\Pi_1$ and $C^1\Pi$ states,

respectively, which are somewhat different than the previously reported values of 67,088 cm^{-1} and 70,528 cm^{-1} [86]. In two previous theoretical studies [92, 93], dynamic electron correlation was deemed important.

Reliable calculations of the HBr electronic states are thus needed in order to characterize unambiguously the nature of the transitions to the higher Rydberg states and to resolve the discrepancies in previously reported data. This is especially important, [79, 80, 94, 95] in light of the difficulties associated with the analysis of the HBr spectra, and because of the relevance to HBr photoionization. For example, the interaction of the intermediate high-energy states with the valence states is known to result in the formation of both atomic and molecular ions products upon photoexcitation. Further, recent experimental work by Castleman and co-workers [34, 96, 97] on HBr in small water clusters also suggested that HBr photoionization is the result of the interaction between Rydberg states and the $V^1\Sigma^+$ion-pair state. The nature of the Rydberg excited states [98, 99], their complex character due to the numerous interstate interactions, characteristic for such large atom as bromine, and the fact that the bonding changes from covalent to ionic as a function of internuclear separation all command the use of multireference methodology [98]. The ground electronic state of HBr has been characterized previously by means of relativistic configuration interaction (CI) [84] and multireference configuration interaction (MRCI) [92] calculations, and the multireference character of the ground-state wavefunction was proven important, even near the equilibrium distance [92].

In this chapter, potential energy curves of the ground, ion-pair and Rydberg states, along with dipole moment curves and the corresponding vibrational levels are characterized for HBr up to the intermediate $E^1\Sigma^+$ state by high-level quantum chemistry calculations. The

outline of this chapter is as follows. The methodology used in this work is described in Section II. The results are presented in Section III along with discussion of the ground-state potential energy curve, the potential energy and transition dipole moment curves for the lowest valence manifold of Π symmetry, and of the low-lying Rydberg and the ion-pair states. Conclusions follow in section IV.

III.2. Computational Details

The internally contracted multireference configuration interaction (MRCI) [100, 101] method as implemented in the MOLPRO package [102] was used to calculate the HBr potential energy curves and transition dipole moments. The reference wave function was generated using a Complete Active Space Self-Consistent Field (CAS-SCF) [103, 104] procedure with an active space consisting of the $6\sigma_{4pz+1s}$, $4\pi_{4p(x,y)}$, $7\sigma^*_{4pz}$, $8\sigma^*_{5s}$ and $5\pi^*_{5p(x,y)}$ molecular orbitals of HBr.

As relativistic effects were previously shown to be significant for large halides such as iodine [105], they were included in the treatment of the K and L shell of the bromine by employing a small-core pseudo-potential, along with a aug-cc-pVTZ-PP correlation-consistent basis set [106, 107] of Peterson and co-workers for the valence electrons, which later in the chapter will be referred to as TZ. The aug-cc-pVTZ augmented correlation-consistent polarized core/valence basis set [108] was used for H. It was shown earlier [109] that including diffuse functions on hydrogen in molecules containing species with a large core such as Br is essential to predict reliable energy minima, spectroscopic and geometrical data for excited electronic states.

Several basis sets were tested. The benchmarking was done on the basis of previously reported experimental values of 3685 cm^{-1} and 30,210 cm^{-1} for the bromine fine-structure splitting $E(^2P_{1/2}) - E(^2P_{3/2})$ [110] and dissociation energy D_0 [111], respectively. It was already proven that the aug-cc-pV5Z-PP basis set provides optimal results for the ground and low-lying valence excited states [92]; This basis set yields a D_0 of 29,349 cm^{-1} (3.0 % error compared to experimental value) and a bromine fine-structure splitting of 3538 cm^{-1} (4.0 % error compared to experimental value), exactly as in [92]. The aug-cc-pVDZ-PP yields a D_0 of 28,154 cm^{-1} (7.3 % error compared to experimental value), a bromine atom fine structure splitting of 3370 cm^{-1} (8.5 % error compared to experimental value); aug-cc-pVTZ-PP yields D_0 of 29,280 cm^{-1} (3.2 % error compared to experimental value) and a bromine fine-structure splitting of 3397 cm^{-1} (7.8% error compared to experimental value). Since the computational demands for calculations of the higher electronic states with inclusion of spin-orbit coupling would be unrealistic with the aug-cc-pV5Z-PP basis set, the aug-cc-pVTZ-PP basis set, which produces results of similar accuracy, is adopted in the following.

Spin-orbit (SO) effects were accounted for via the effective one-electron spin-orbit operator included in the relativistic effective core potential of bromine. Calculations of the potential energy curves corrected for SO coupling were performed with the interacting-states method as implemented in the MOLPRO package [102]. The spectroscopic properties of selected electronic states of HBr, such as vibrational energies (G_v) and rotational constants (B_e), were calculated from the ab initio potential energy curves with the LEVEL program [112].

III.3 Results and Discussion

The calculations are carried out in C_{2v} symmetry. The reason for this is that the MOLPRO package can use Abelian point group symmetry only. Therefore, for molecules with degenerate symmetry, such as linear molecules ($C_{\infty v}$), Abelian subgroup C_{2v} is implemented [102]. A total of 14 molecular orbitals (MOs) ($1\sigma_{3s}$, $2\sigma_{3pz}$, $1\pi_{3px,y}$, $3\sigma_{3d}$, $2\pi_{3d}$, $4\sigma_{3d}$, $1\delta_{3d}$, $3\pi_{3d}$, $5\sigma_{4s}$) $6\sigma_{4pz+1s}$, $4\pi_{4px,y}$, $7\sigma_{4pz}$*, $8\sigma_{5s}$*, $5\pi_{5px,y}$* are treated explicitly aside from the 5 inner most atomic-like MOs (*core* = [σ_{1s}, σ_{2s}, σ_{2pz}, π_{2px}, π_{2py}]) corresponding to the K and L shells of Br which are accounted for by a pseudopotential as mentioned above. The active MOs used in this calculations in order to generate the valence and Rydberg electronic states, i. e. $6\sigma_{4pz+1s}$, $4\pi_{4px,y}$, $7\sigma_{4pz}$*, $8\sigma_{5s}$*, $5\pi_{5px,y}$* are separated by symmetry as follows: 3 of A_1, 2 of each B_1 and B_2 elements of irreducible representation. The most important MOs that contribute to the excited states discussed in this chapter are depicted in Figure 10. The $A^1\Pi$ and $a^3\Pi$ manifolds originate from the $4\pi^4 \rightarrow 7\sigma^*$ transition, the $C^1\Pi$ and $b^3\Pi$ states from the $4\pi^4 \rightarrow 8\sigma^*$ transition, the first excited sigma states $V^1\Sigma^+$ and $t^3\Sigma^+$ states from the $6\sigma^2 \rightarrow 7\sigma^*$ and the $E^1\Sigma^+$, and $e^3\Sigma^+$ states from the $4\pi^4 \rightarrow 5\pi^*$ transitions. The potential energy curves for all 10 states consisting of three singlet $^1\Sigma^+$ (A_1) – ($X^1\Sigma^+$, $V^1\Sigma^+$, and $E^1\Sigma^+$), two singlet $^1\Pi$ (B_1+B_2) – ($A^1\Pi$, $C^1\Pi$), one triplet $^3\Sigma^+$ (A_1) – ($t^3\Sigma^+$), two triplet $^3\Pi$ (B_1+B_2) – ($a^3\Pi$, $b^3\Pi$) and one singlet $^1\Delta$ (A_1+A_2) – $F^1\Delta$ state are shown in Figures 11 and 13, while the molecular orbital configuration of these states is given in Table 6 and the transition dipole moments are shown in Figure 12 and 14.

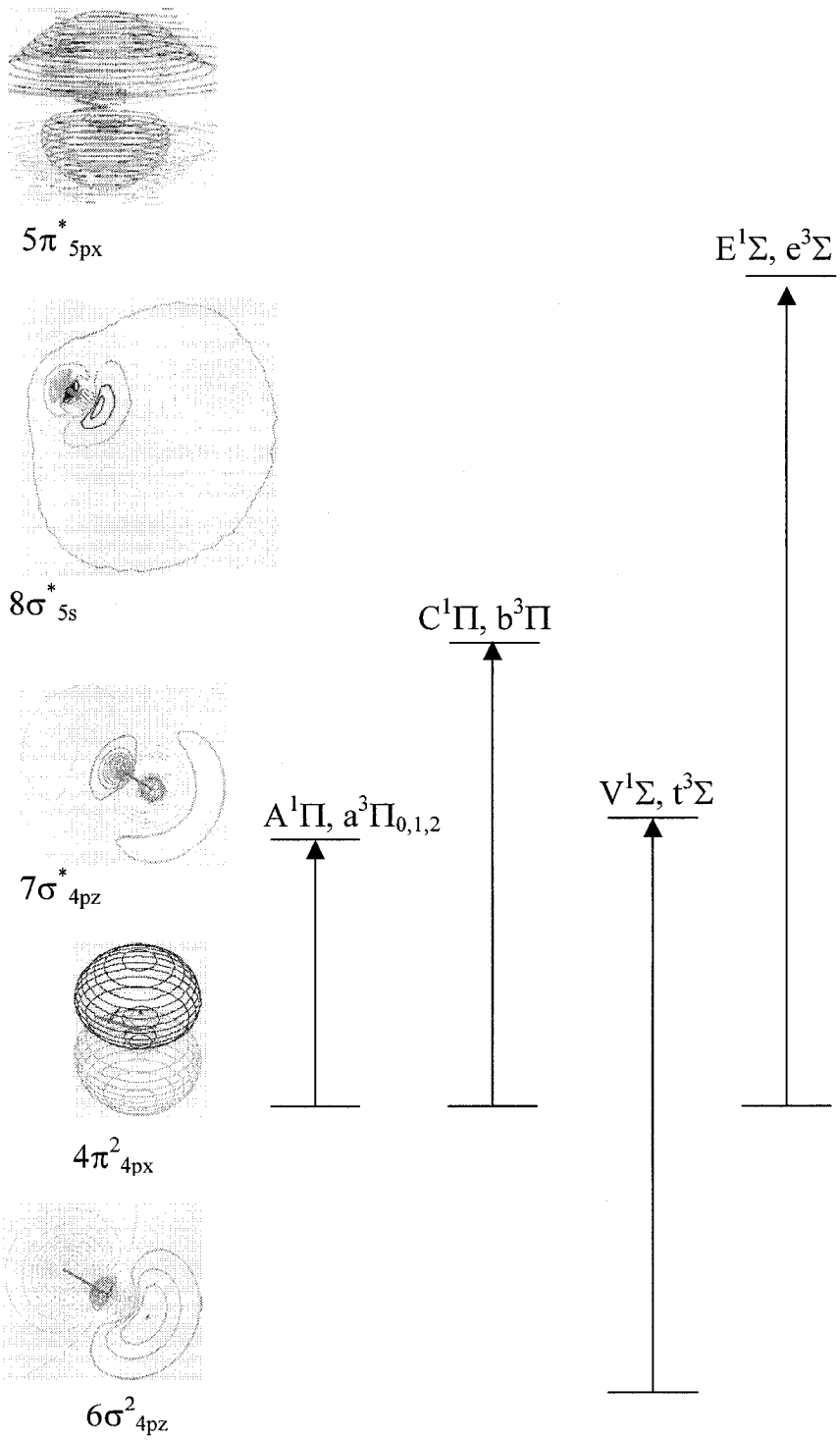

Figure 10: Molecular orbitals of HBr contributing to the electronic states, discussed in this work.

Table 6: Spectroscopic assignment of HBr electronic states and molecular configurations [a]

MO configuration	Ginter's notation
$(\sigma^2\pi^3)\sigma^{*1}$	a $^3\Pi_i$ (0,1,2), A $^1\Pi$(1)
$(\sigma^1\pi^4)\sigma^{*1}$	t $^3\Sigma^+$ (0^-,1), V $^1\Sigma^+(0^+)$
$(\sigma^2\pi^3)5s\sigma^1$	b $^3\Pi_i$ (0,1,2), C $^1\Pi$(1)
$(\sigma^2\pi^3)5p\sigma^1$	d $^3\Pi_i$ (0,1,2), D $^1\Pi$(1)
$(\sigma^2\pi^3)5p\pi^1$	e $^3\Sigma^+$ (0^-,1), E $^1\Sigma^+(0^+)$
	f $^3\Delta_i$ (1,2,3), F $^1\Delta$(2)
$(\sigma^2\pi^3)5d\sigma^1$	n $^3\Pi_i$ (0,1,2), N $^1\Pi$(1)

[a] The notation of reference [85] is adopted.

III.3.a. The HBr ground electronic state.

The ground-state wave function of HBr predominantly involves a (core...$5\sigma_{4s}$) $6\sigma_{4pz+1s}$,$4\pi_{4px,y}$ configuration near the equilibrium internuclear distance. The dissociation energy (D_0) calculated here (Table 7) is in an excellent agreement with the experimental value of 3.74 eV [111]. The lowest vibrational level of the ground state, listed in Table 8, was calculated to be 2643 cm^{-1}, which agrees very well with the previously reported experimental value of 2648 cm^{-1} [92].

III.3.b. HBr excited electronic states of Π symmetry.

The potential energy and transition dipole moment curves for the low-lying valence excited states of HBr are shown in Figures 11 and 12, respectively. The repulsive $a^3\Pi$ and $A^1\Pi$ valence states, which originate from the (core...$6\sigma^2$,$4\pi^3$)$7\sigma^{*1}$ molecular configuration, form the lowest dissociation channel following excitation from the ground state. It was shown earlier for HF [113], HCl [114-116], HI [117, 118] and HBr [91, 119, 120] that upon photoexcitation, the ground the low-lying repulsive electronic states of

Table 7: Properties of HBr electronic states [a]

State	T_{vert} [b]	Other work	μ [c] MRCI	Other work	D_0 [d] MRCI	Other work
$X^1\Sigma^+$	0	0	0.77	0.82 [e]	3.72	3.76 [e]
$a\ ^3\Pi$	49,326	-				
$A^1\Pi$	54,862	56,500 [f]	0.35			
$b\ ^3\Pi$	68,366	67,088 [i]	-1.87	-1.75		
$C^1\Pi$	70,188	74,889 [e]	-2.89	-1.95		
		70,527 [h]				
$t^3\Sigma^+$	71,462	-	0.99			
$V^1\Sigma^+$	75,310	75,923 [g]	1.16			
$d\ ^3\Pi$	74,266	73,542 [i]	3.35			
$D^1\Pi$	75,507	76,198 [i]	-0.89			
$e^3\Sigma^+$	73,580	73,740 [h]	1.12			
$E^1\Sigma^+$	76,478	77,939 [i]	0.81			
$f\ ^3\Delta$	74,871	74,221 [i]	1.12			
$F^1\Delta$	75,522	77,009 [i]	1.16			
$n\ ^3\Pi$	79,319	-	-3.78			
$N^1\Pi$	81,509	81,309 [j]	0.28			

a. All values given at the ground state equilibrium distance (r_e = 1.42 Å).
b. Vertical Franck-Condon energies in cm^{-1}, calculated with MRCI/aug-cc-pVTZ.
c. Dipole moment in D, calculated with MRCI/ aug-cc-pVTZ.
d. Dissociation energy in eV, calculated with MRCI/ aug-cc-pVTZ.
e. From reference 6.
f. From reference 46.
g. From reference 47.
h. From reference 8.
i. From reference 7.
j. From reference 45.

HX interact via spin-orbit coupling resulting in the photo-fragments H(^{2}S) and X(^{2}P), and the relative branching ratios of the various fragments have been reported, providing invaluable

information on the photodissociation process. It was shown that when spin-orbit coupling is taken into account, there are two dissociation channels $H(^2S_{1/2})$ + Br $(^2P_{3/2})$ and $H(^2S_{1/2})$ + Br $(^2P_{1/2})$, involving the ground and four optically accessible spin-orbit excited states, respectively [92]. The vertical Franck-Condon energy for the valence singlet $A^1\Pi$ state is calculated to be 54,862 cm^{-1}, which is in good agreement with the previously reported experimental value of 56,500 cm^{-1} [78] (error of 3.0 %). As can be seen from the transition dipole moment curves in Figure 12, all four optically accessible states of the $A^1\Pi$ and $a^3\Pi$ manifolds can contribute to initial excitation, with the least contribution from the $t^3\Sigma$ states.

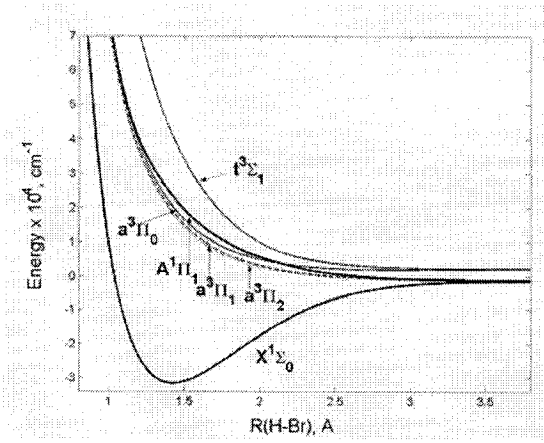

Figure 11: Potential energy curves of the valence $^1\Pi$, $^3\Pi_i$, and $^3\Sigma^+$ manifolds of HBr from MRCI/aug-cc-pVTZ calculations including spin-orbit coupling.

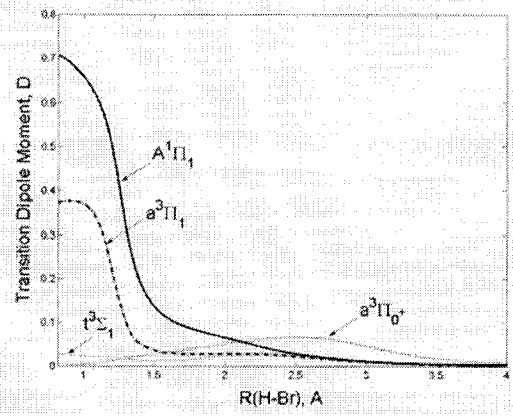

Figure 12: Transition dipole moment curves for the $X^1\Sigma^+$ to the valence $A^1\Pi$, $a^3\Pi$ and $t^3\Sigma$ states from MRCI/aug-cc-pVTZ calculations.

The potential curve of the lowest Rydberg $C^1\Pi$ state, shown in Figure 13, has a minimum at an internuclear separation of 1.52 Å. The shift from the ground-state equilibrium distance of 1.42 Å is caused by perturbations from the valence (core...$6\sigma^2$,$4\pi^3$)$7\sigma^{*1}$ manifold. The $C^1\Pi$ state is of primary interest as it was implicated

in recent experiments on HBr photoionization in water [97] and because of difficulties of estimating spin-orbit coupling with the $A^1\Pi$ and $a^3\Pi$ manifolds and rovibrational structure. The calculated first four rovibrational levels are reported in Table 8. However only the band of the $D^1\Pi$ state was reported previously [85]. Due to weak spin-orbit coupling, signals from the $b^3\Pi$ and $C^1\Pi$ states could not be observed [85] as for the $D^1\Pi$ state. As can be seen from Figures 12 and 14, the transition dipole moment for the transition from the ground state to the $C^1\Pi$ state indicates that it is accessible at much higher energies than the $t^3\Sigma$ state and the repulsive-valence manifolds. Further, from the relative position of the potential curve and the previous report [114] of its rotational coupling to the $F^1\Delta$ state, the $C^1\Pi$ states may acts as a gateway for predissociation of the F-state, as discussed later.

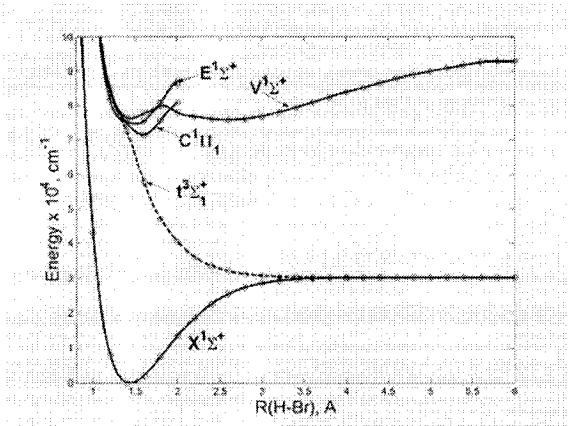

Figure 13: Potential energy curves of the ground $X^1\Sigma^+$, valence $t^3\Sigma$, Rydberg C $^1\Pi$ and $E^1\Sigma^+$, and ion-pair $V^1\Sigma^+$ states of HBr from MRCI/aug-cc-pVTZ calculations including spin-orbit coupling.

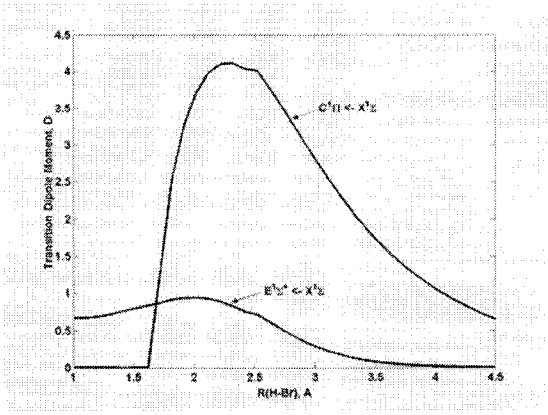

Figure 14: Transition dipole moment curves for (a) the $X^1\Sigma^+$ ground electronic state to the valence $A^1\Pi$, $a^3\Pi$ and $t^3\Sigma$ states and (b) the $X^1\Sigma^+$ ground electronic state to the Rydberg $C^1\Pi$ and $E^1\Sigma$ states, from MRCI/aug-cc-pVTZ calculations.

III.3.c. HBr excited electronic states of Σ and Δ symmetry

Although originating from different molecular orbital configurations, the states from the (core...$6\sigma^1$,$4\pi^4$)$7\sigma^{*1}$ and (core...$6\sigma^2$,$4\pi^3$)$5\pi^{*1}$ manifolds undergo avoided-crossing perturbations, which result in the formation of a double-well potential for the ion-pair $V^1\Sigma^+$ state and the corresponding potential energy curves are reported in Figure 13. The MRCI vertical T_v energies (Table 7) compare very well to the experimental data reported in [86, 121]. The transition and permanent dipole moments are shown in Figure 14 and 15. The correct description of the potential energy curves of these manifolds requires a proper treatment of spin-orbit coupling. All low-lying Rydberg $^{1,3}\Sigma^+$ and $^{1,3}\Pi$ states form a manifold well above the ground state, as can be seen in Figures 13 and 16, and therefore all mix because spin-orbit coupling. For example the $F^1\Delta$ and $f^3\Delta$ state coincide with the ion-pair

$V^1\Sigma^+$ state near the ground-state equilibrium HBr distance up to a distance of 2.0 Å, while the intermediate $E^1\Sigma^+$ and the valence ion-pair curves give rise to an avoided crossing between

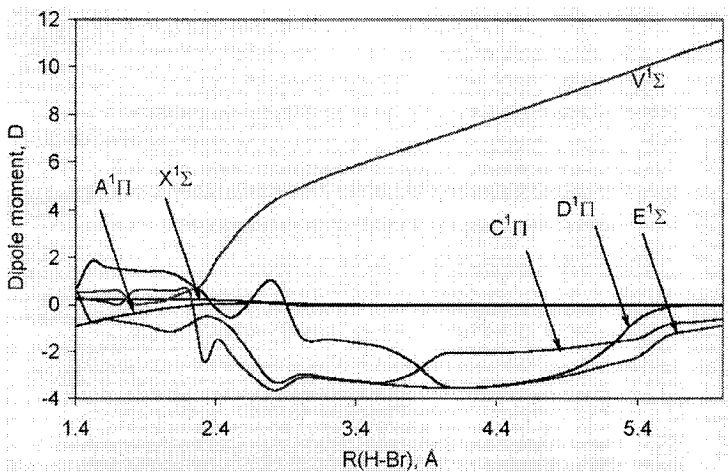

Figure 15: Dipole moment curves to the ground $X^1\Sigma^+$, valence $A^1\Pi$, ion-pair $V^1\Sigma^+$ and Rydberg $C^1\Pi$ and $E^1\Sigma$ states, from MRCI/aug-cc-pVTZ calculations.

1.9 and 2.0 Å. Thus, based on the calculated potential curves, a barrier height of 16.2 kcal/mol, at 1.92 Å between the two wells of the ion-pair state is obtained for the first time. In this study, the attention is focused on properties of the $C^1\Pi$, $E^1\Sigma$ and $V^1\Sigma$ states, since they are involved in photoionization of HBr. In order to explain the latter, permanent and transition dipole moments were calculated with respect to internuclear HBr separation. In Figure 14, the transition dipole moments of both $C^1\Pi$ and $E^1\Sigma$ states show that they are optically accessible, however from the vertical energy of the $E^1\Sigma$ state, 76,471 cm^{-1} one can conclude that it is much less energetically favorable with respect to the $C^1\Pi$ state, 70,188 cm^{-1} as it can be seen from Table 8.

The dipole moments reflect the electronic charge distribution and thus help characterize the HBr electronic structure in various electronic states. In general, CASSCF

predicts dipole moments that compare well to experimental results [99], and for instance, Buenker and co-workers [98] reported very good agreement between the CASSCF dipole moments of the HI ground and $a^3\Pi$ states with experimental data. As for HBr, Chapman and co-workers [14] observed the same trends in the dipole moments for the ground, $a^3\Pi$ and $V^1\Sigma^+$ manifolds as in the present work. Even though the method (restricted CI or RCI) used in [84] does not account for dynamic electronic correlation energy the results and discussion of the ground-state dipole moment could be used as a reference. Although generally the Rydberg $C^1\Pi$ and $E^1\Sigma$ are listed in the literature as bound-covalent states [85, 88], the plot of the dipole moments (Figure 15) suggest that due to their extensive mixing with the ion-pair state, these states change polarity in the region of the avoided crossing and their negative dipoles reflect slightly ionic nature up to 5 Å when their dipoles decay to zero, indicating their bonding character. Contrary to the Rydberg, the ion-pair state is characterized with a largely positive dipole, indicating that electron density is shifted away from H towards Br upon internuclear separation and from the potential energy curve (Figure 13) it can be seen that it is nonbonding state as assumed earlier [85] base on comparison with the HCl ion-pair state. This analysis is important in relation to the vibrational spectra discussed later, as it rationalizes the uneven distribution of their vibrational levels.

III.3.d. Spectroscopic properties of the HBr low-lying Rydberg and ion-pair states

The results obtained from MRCI calculations with spin-orbit coupling for the vibrational levels of the intermediate and ion-pair states are listed in Table 3. Energies of the first 4 vibrational levels of the $C^1\Pi$ state are reported for the first time. Those energies of the

vibrational levels of the $E^1\Sigma$ and $V^1\Sigma$ which were available in the literature [85, 89] were used in this study for reference and to obtain the correct order of

Table 8: Calculated rovibrational spectroscopic constants for the $C^1\Pi$, $V^1\Sigma^+$ and $E^1\Sigma^+$ states

State	υ [a]	G_v [a]	r_{inner} [b]	r_{outer} [b]	B [c]	D x 10^3 [c]	(m+) $G_{vexp.}$ Other work [d]
$X^1\Sigma^+$	0	2643	-	-	-	-	(0) 2648
$C^1\Pi$	0	70 493			7.75		
	1	72 387	1.32	1.82			
	2	75 929	1.26	2.00			
	3	79 197	1.20	2.17			
$V^1\Sigma^+$	0	75 548	1.41	1.46	2.35		(0) 75 923
	1	76 078	2.46	2.99	2.27		(1) 76 514
	2	76 589	2.37	3.06	2.74		(2) 76 962
	3	77 383	2.36	3.18	3.2	-5	(3) 77 345
	4	78 232	2.24	3.42	3.2		(4) 77 821
	5	78 471	1.29	1.68	3.55		(5) 78 390
	6	79 027	2.19	3.54	3.72	2.2	(6) 78 941
	7	79 770	2.14	3.65	4.01	7.5	(7) 79 481
	8	80 350	2.14	3.75	3.96	14	(8) 80 028
	9	80 543	1.23	1.75	4.38		(9) 80 646
	10	81 145	2.10	3.84	3.61	-1	(10) 81 194
	11	81 759	1.23	1.81	5.75	-11	(11) 81 684
	12	82 337	2.00	4.08	5.12	3.5	(12) 82 418
	13	82 878	1.23	4.14	5.07	6.8	(13) 82 915
							(14) 83 777
$E^1\Sigma^+$	0	77 313	1.37	1.74			(0) 77 940
	1	80 076	1.26	1.86			(1) 80 168
	2	82 143	1.26	1.96			(2) 82 274
	3	83 273	1.24	2.00			(3) 84 250
	4	86 846	1.18	2.20			(4) 86 132

a. Vibrational levels υ and energies G_v, in cm^{-1}.
b. Potential energy curve turning points, in Å.
c. Rotational constants B and D, in cm^{-1}.
d. From reference [89].

these levels since experimentally they are only assigned relatively, by m+0 assuming that the experimentally detected level might not be the lowest available for a particular electronic

state. Thus the $G_{v=3}$ (77,383 cm^{-1}), $G_{v=5}$ (78,471 cm^{-1}) and $G_{v=1}$ (80,078 cm^{-1}) and $G_{v=3}$ (83,273 cm^{-1}) of the $V^1\Sigma$ and $E^1\Sigma$, respectively are in very good agreement with previously reported values from experiment [85, 89]. Since only the low-lying vibrational

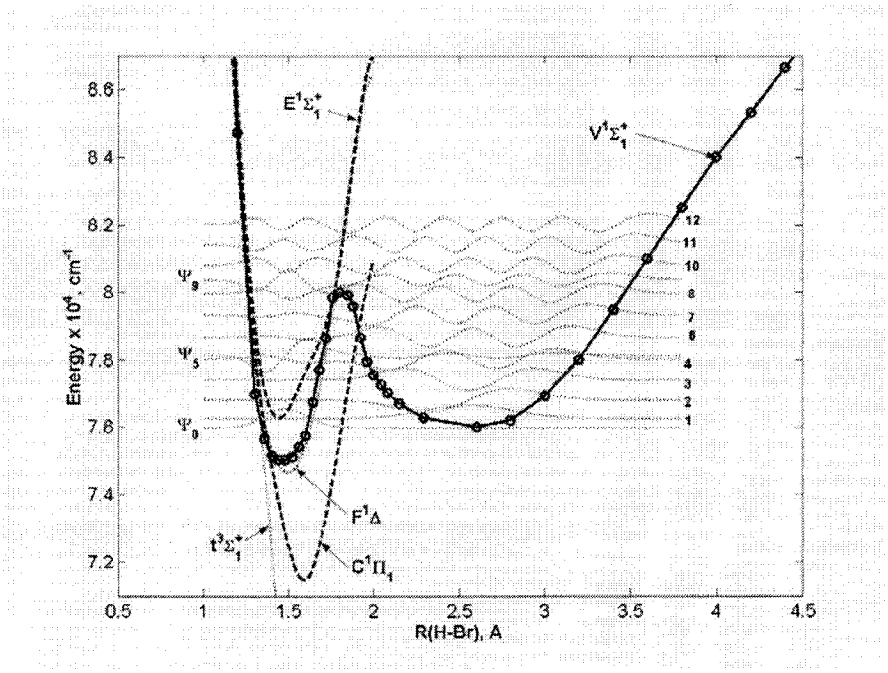

Figure 16: Potential energy curves from MRCI/aug-cc-pVTZ calculations of the lowest Rydberg $C^1\Pi$ state, the intermediate $E^1\Sigma^+$ and the valence ion-pair $V^1\Sigma^+$ states along with the vibrational levels (v'=0-13) of the former.

energies are well documented [85], potentials curves for these three states have not been reported to date, which till recently leaves uncertain the mechanism of interaction of these states leading to the formation of the ion-pair state.

Our calculations indicate that the vibrational levels of the ion-pair state are rather unevenly distributed, as was proposed previously [88, 89] on the basis of their energies and possibly due to spin-orbit coupling known to be characteristic for this state. The turning points, listed in Table 8 show alternation of the vibrational levels between the two wells of the potential. Further, the first calculated thirteen vibrational levels of the ion-pair state and

the first four levels of the intermediate $E^1\Sigma^+$ agree with the only reported data [89] and are used along with the newly calculated first four levels of the Rydberg $C^1\Pi$ states to explain mutual perturbations in these vibrational spectra, discussed below. As can be seen from vibrational levels listed in Table 8, the spacing of levels of the Rydberg E- and C-states is significant in contrast to compression of the vibrational levels in the V-states. This was previously attributed to the repulsive homogeneous interaction between the Rydberg E- and the ion-pair V-states [89, 90]. The former are due to interactions of the m+0 and m+1 with $\upsilon'_C = 2$, between m+4 and m+5 interacting with $\upsilon'_E = 0$, between m+6 and m+7 due to interaction with $\upsilon'_C = 3$ and between m+8 and m+9 due to interaction with $\upsilon'_E = 1$. The position in the double-well potential of the V-state vibrational levels can be determined from the calculated turning points (Table 8). Since the energy barrier of this state is near the $\upsilon'_E = 3$ level, higher vibrational levels of the V-state as well as for the E- and C- states were not calculated. Also since $\upsilon'_V = 0$ is much lower than the barrier and the spacing of the higher vibrational levels are larger than the bandwidth of the pump laser [96] and therefore they cannot be populated, a tunneling mechanism is expected to govern the ionization dynamics of HBr.

III.4. Conclusions

In this chapter, ab initio calculation of the HBr potential energy curves are reported for the ground, valence (repulsive), and the low-lying Rydberg states in the vicinity of the ion-pair $V^1\Sigma^+$ state accompanied with complete list of the bound-state vibrational levels of the Rydberg states which serves to explain their interaction. For the correct interpretation of all states considered in this chapter, the vertical excitation energies were calculated at the

equilibrium distance and it was found that they compare well to available experimental values. Contour plots of the most important molecular orbitals involved in the electronic transitions considered in this chapter were shown in order to support the discussion on the nature of these transitions. It was shown that spin-orbit coupling is very well pronounced for the ground and valence (repulsive) manifolds, showing that this effect must be included in the calculation of the potential energy curves and transition dipole moments for the $A^1\Pi$ and $a^3\Pi$ manifolds as well for the Rydberg $C^1\Pi$ and $E^1\Sigma$, and for the ion-pair $V^1\Sigma$ states. It was demonstrated through the transition dipole moments that when spin-orbit states were considered, all optically accessible $A^1\Pi$, $a^3\Pi$, and $t^3\Sigma$ states contribute to the initial excitation from the ground state. Including spin-orbit effects in the calculation of the low-lying Rydberg and ion-pair states was especially important due to their extensive perturbation at a long range of internuclear distances and in the explanation of the uneven distribution of the vibrational levels in these states. The transition dipole moments of these states were used to distinguish the nature of the ion-pair state. The potential energy barrier of the ion-pair state between the two wells was calculated to be 16.2 kcal/mol, a value suggesting that tunneling mechanism of the ionization of HBr from this state should be considered.

Chapter IV.

On the Photoionization of HBr in Water Clusters

To be submitted as:

Sacha Z. Zlatkova and Gilles H. Peslherbe, *Journal of Chemical Physics (Communications)*, (2007)

IV.1 Introduction

The photoionization and photodissociation of a typical molecule is a multiphoton and a multicontinuum processes [122]. In studies with weak visible or ultraviolet radiation, a molecule absorbs a single photon and dissociates on the lowest potential energy surface accessible within the Franck-Condon window. Upon excitation, the population of the neutral excited state, AB**, can decay either by predissociation to form A + B* or $A^+ + B^-$, or by autoionization to form $AB^+ + e^-$. The photoionization of hydrogen halides, hydrogen bromide (HBr) in particular, in water clusters has been a matter of discussion in relation to their possible role in the ozone layer depletion problem [123-125]. Gas-phase HBr by itself has been the subject of numerous experimental and theoretical investigations, which have revealed a detailed picture of the photodissociation process leading to atomic products [79, 85].

$$HBr(X^1\Sigma^+) + h\nu \rightarrow HBr^*(A^1\Pi) \rightarrow H(^2S) + Br(^2P_{1/3,2/3}),$$

It was shown that all three lowest-valence $A^1\Pi$, $a^3\Pi$ and $t^3\Sigma$ manifolds are optically accessible and thus can contribute to HBr photodissociation [92]. However, multiphoton excitation allows population of a series of Rydberg and higher excited states of HBr [85, 88, 90], and depending on the nature of the excited state populated and its interaction with neighboring states, photoionization may occur in one step, leading to the production of ions

$$HBr(X^1\Sigma^+) + h\nu \rightarrow HBr^*(4p\pi) \rightarrow H^+ + Br^-$$

or a more complex autoionization process may occur which is not replicated in the present study and thus not discussed.

The dissociation of strong acids such as a hydrogen halide in water is a fundamental process for understanding the nature and behavior of hydration, which results in the

formation of ion pairs. It was also anticipated that solvent fluctuations may play an important role in the photoionization of hydrogen halides [36]. It was postulated that, in the presence of water, ground-state HBr does not ionize in clusters of different size, but photoionization upon photoexcitation (to yield $H^+ + Br^-$) might be possible in water clusters as the HBr ion-pair state, formed as a result of the avoided crossing between the first-excited and Rydberg singlet states ($V^1\Sigma^+$ and $E^1\Sigma^+$ [83, 89, 90, 126]) could become energetically and optically accessible. The fundamental experimental work of Castleman and co-workers [125] is the only study of HBr photoionization in water clusters reported to date, in which an ultrafast dynamics experiment was performed using pump-probe techniques and reflection time-of-flight mass spectrometry. The interpretation of the experimental results is rather convoluted. For gas-phase HBr, a small absorption cross-section for the ion-pair $V^1\Sigma^+$ state was reported, inferring a very low probability of photoionization. However, an increase in the signal of ionized species was found in the presence of water molecules about the ion core. Castleman and co-workers concluded that solvent motion leads to an increase in the absorption cross-section, and thus the observed ion signal. They also found that a minimum of five water molecules were necessary for the formation of a contact ion pair (CIP). A series of theoretical studies [28, 29, 43, 44, 127], however, unambiguously showed that a cluster of four water molecules is sufficient to cause HBr ground-state ionization, leading to the formation of a CIP, and ultimately a solvent-separated ion pair (SSIP). None of these studies dealt with the behavior of these complexes upon photoexcitation, a key step to thoroughly understand and interpret the experimental results.

In the present chapter, we report an investigation of the effects of solvation on excited-state HBr ionization. The outline of this chapter is as follows. The computational

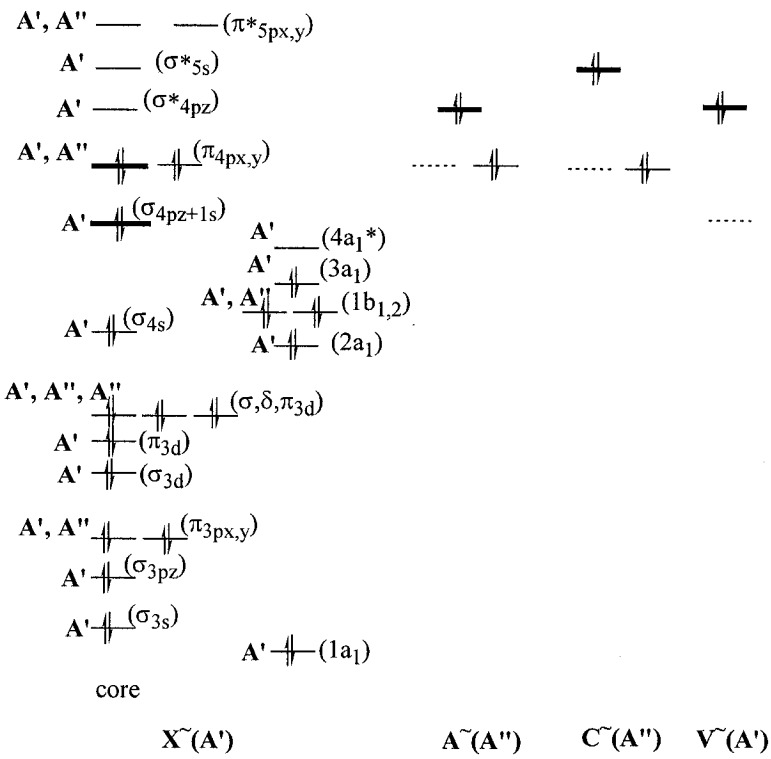

Figure 17: Electronic configuration of the ground, Rydberg, and ion-pair singlet states of HBr(H_2O). The $3a_1$, $1b_1$ and $4a_1$ molecular orbitals of water interact with the π_{4pz} molecular orbital of HBr and form 4 mixed molecular orbitals of A' symmetry in the C_s complex. The *core* contains the 1s, 2s and 2p molecular orbitals of Br embedded in the small-core pseudopotential.

methodology employed in this work is first presented in Section II. The results of our calculations (molecular structures, potential energy and dipole moment curves of the lowest Rydberg and ion-pair states, ionization potentials, Franck-Condon vertical energies and differential solvation energies) are then presented for $HBr(H_2O)_n$ (n = 0 - 4) in Section III. A summary and conclusions follow in Section IV.

IV.2. Computational Details

The ground and excited-state electronic structure of $HBr(H_2O)_n$ were calculated using the state-averaged complete active space self-consistent field (CAS-SCF)

formalism [128, 129] as implemented in MOLPRO [102]. A small-core relativistic pseudopotential was used for the inner K, L, and M shells of bromine, in combination with the aug-cc-pVDZ-PP augmented correlation-consistent basis set [130], while Dunning's aug-cc-pVDZ correlation-consistent double-zeta basis set [108, 131] was used for hydrogen and oxygen. The active space for the $HBr(H_2O)_n$ complexes is constructed according to the scheme depicted in Figure 17 for $HBr(H_2O)$. As separate species, the molecular orbitals (MOs) of both HBr and H_2O belong to a irreducible representation of C_{2v} symmetry, while the MOs of each $HBr(H_2O)$ belong to a representation of lower symmetry C_1 (C_s symmetry was used initially for identification of the electronic structure of the states below the ion-pair state). Therefore, as can be seen from Figure 17, all σ MOs are represented as A'(A) orbitals, the π orbitals comprise one A' and one A" orbital, and the 3d orbitals three A' and two A" orbitals. CAS-SCF/aug-cc-pVDZ-PP is computational-cost effective, and allows treatment of systems as large as $HBr(H_2O)_n$ (n=1-4), while producing total energies within 7% error of the MRCI/aug-cc-pVTZ method used in Chapter III for gas-phase HBr.

The electronic configuration of the $HBr(H_2O)$ complex $X^{\sim}(A')$ ground state is characterized by a $[\sigma^2_{4pz}\pi^4_{4px,y}]$ valence configuration. In order to probe the effects of water on the excited states of HBr, only excitations to the valence $A'(\sigma^{*0}_{4pz})$ and $A'(\sigma^{*0}_{5s})$ HBr orbitals are taken into account in this calculation, which represents an active space of 6 electrons in 7 molecular orbitals. In order to preserve this active space for the larger clusters, where symmetry cannot be used, subsequent inspection of the molecular orbitals and comparison of the results for vertical energies of HBr for C_{2v} and C_1 symmetry showed that transitions from the ground to the first four excited states

comprises the spectrum of HBr in water up to its lowest ion-pair state limit. The ground-state geometries of $HBr(H_2O)$ structures were optimized at constrained HBr internuclear separations with the methodology described above, and the resulting structures are shown in Figure 18.

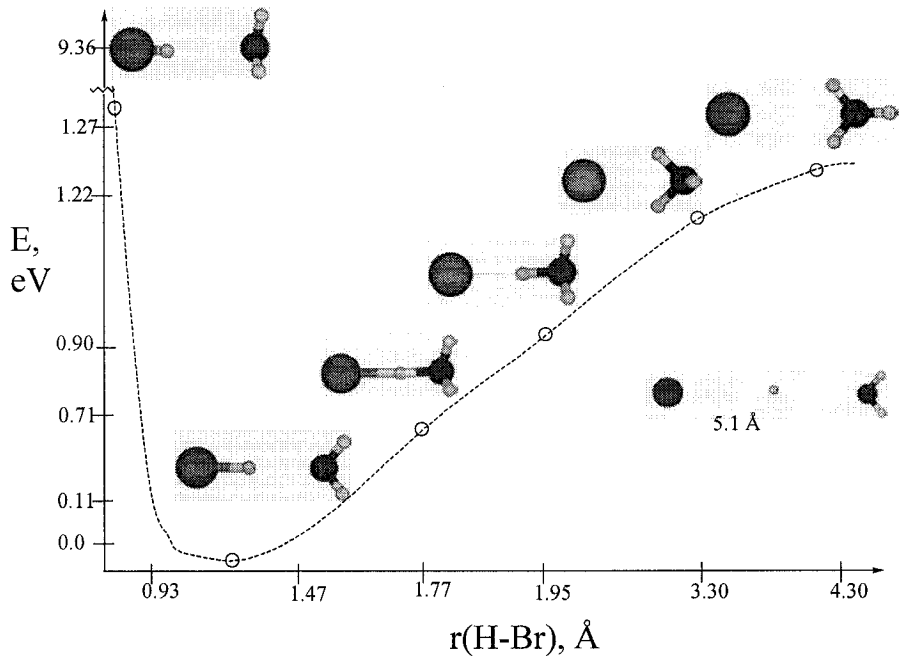

Figure 18: Potential energy curve of the ground $X^{\sim}\Sigma$ state $HBr(H_2O)$ as a function of H-Br internuclear separation, calculated with CAS-SCF/aug-cc-pVDZ.

It was previously predicted theoretically [28, 29, 43, 44, 127] that SSIP forms in a cluster of four water cluster for HBr in its ground electronic state. However, in all those studies a stationary state structure of only particular kind of cluster ($HX(H_2O)_n$, n=1-4 and their ionized alternative forms) was considered in contrast to the dynamic study where different sizes cluster mixture was experimentally investigated at a finite temperature [125]. That is probably the origin of the discrepancy on the number of water

molecules to fully ionize the acid. Based on our previous study [127] of the electron density distribution in all the clusters (n = 0 – 4), we showed that for the two most stable four-water clusters the bromine interacts with the water cluster in a purely ionic fashion. This suggests that the mechanism of ionization of HBr in a four water cluster might involve a combination of CIP formation in the HBr ground electronic state, which transforms into SSIP in the ion-pair state upon excitation due to further solvent fluctuations.

IV.3. Results and Discussion

The ground-state potential energy as a function of the acid internuclear separation is shown in Figure 18. The motion of the water is wobbling with respect to the axis of the acid up to a 1.77 Å internuclear separation, when H_3O^+ starts to form and rotated, forming a contact ion pair (CIP $Br^-\cdot H_3O^+$) at 3.33 Å. This is consistent with previous studies on the dynamics of HCl ionization in water [36], which showed that the reorganization of the water molecules about the ion core initiates the formation of a solvated contact ion pair (CIP), and further solvent fluctuations lead to the formation of solvent-separated ion-pair (SSIP) and thus complete ionization.

The calculated Franck-Condon energies from the potential energy curves, shown in Figure 19, are 8.70 eV and 9.36 eV for the excited $C^1\Pi$ is the ion pair $V^1\Sigma$ states, respectively, and are in good agreement with our previously reported values [126], calculated with MRCI/aug-cc-pVTZ. The $X^{\sim}(A')$ ground state of the acid water complex, as can be seen from Figure 19, is stabilized by 0.19 eV, compared to gas-phase HBr. A stabilization of 0.34 eV and 1.02 eV are calculated for the excited $C^{\sim}(A'')$ and ion-pair

V˜(A') states, respectively. Calculated dipole moments, shown in Figure 20, confirm the covalent nature of the ground state of

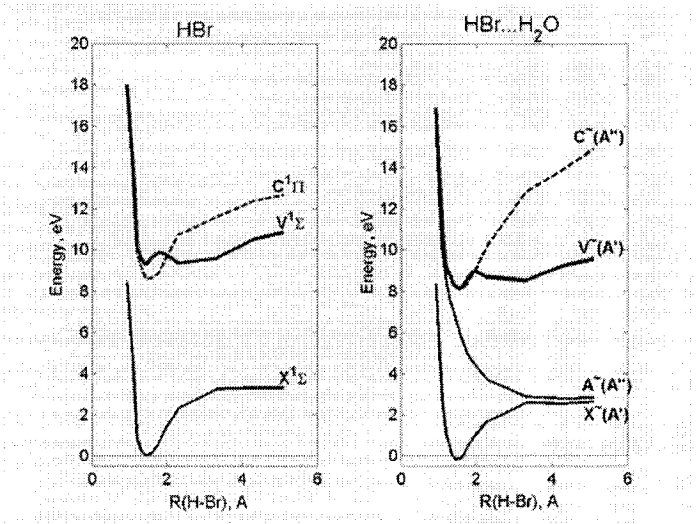

Figure 19: Potential energy curves for the ground $X^1\Sigma^+$, first excited $C^1\Pi$ and ion-pair $V^1\Sigma^+$ states of HBr (left panel), and the ground $X^-(A')$, first excited $C^-(A")$, and ion-pair $V^-(A')$ states of HBr(H_2O) (right panel), calculated with CAS-SCF/aug-cc-pVDZ.

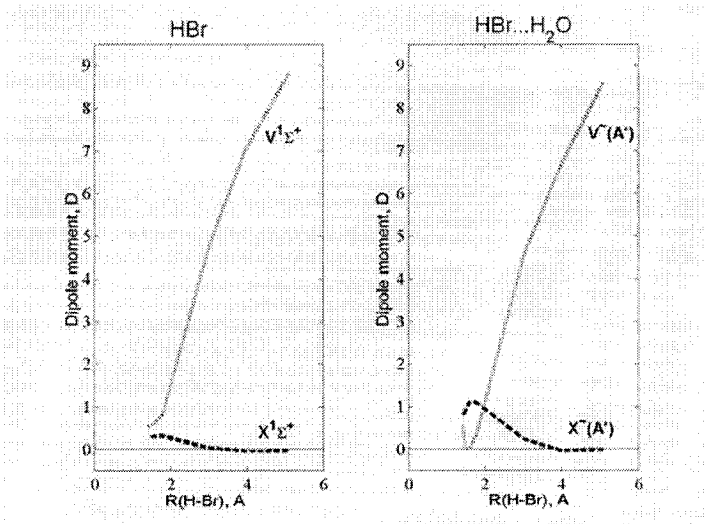

Figure 20: Dipole moment curves for the ground electronic $X^1\Sigma^+$ and ion-pair $V^1\Sigma^+$ states of HBr (left panel) and HBr(H_2O) (right panel), calculated with CAS-SCF/aug-cc-pVDZ.

both HBr and $HBr(H_2O)$, as the dipole moment gradually vanishes as the Br + H + H_2O are formed, and the ionic nature of the ion-pair $V^-(A')$ state as the dipole moment steadily increases for both HBr and $HBr(H_2O)$ as a function of internuclear separation as the products $Br^- + H^+ + (H_2O)_n$ are formed. Thus the water molecule influences all electronic states of HBr involved in the photodissociation, but mostly stabilizes the ion-pair state.

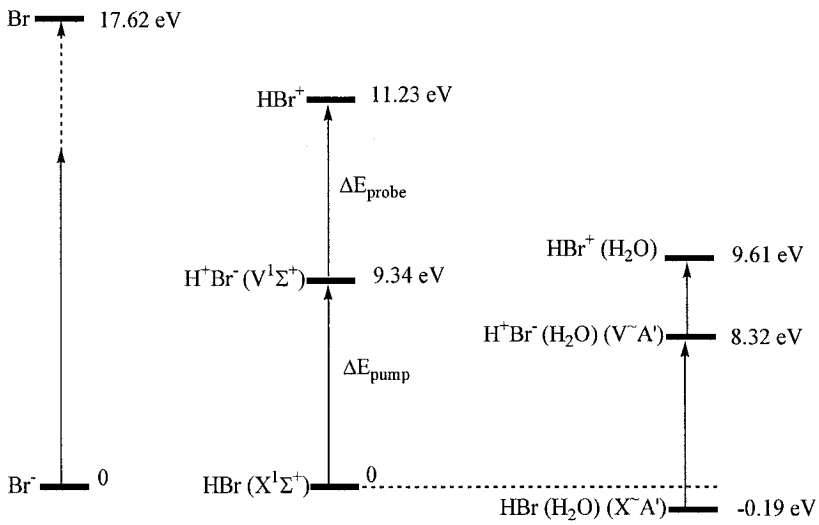

Figure 21: Relative position of the electronic states of Br, HBr and $HBr(H_2O)$, calculated with CAS-SCF/aug-cc-pVDZ.

Comparison of ionization potentials and Franck-Condon energies for excitation to the ion-pair state for HBr and $HBr(H_2O)$ are presented in Figure 21. A reduction of 0.7 eV was estimated earlier (with MP2/6-31G) [125] for the ionization potential (IP) of $HBr(H_2O)$ with respect to that of gas-phase HBr, because of solvent effects. Including dynamic electron correlation yields a value of 1.6 eV for difference in IPs, as the IP for gas-phase HBr is 11.23 eV while the corresponding value for the $HBr(H_2O)$ is 9.61 eV, just 1.3 eV higher than the energy to access the ion-pair V^- state. Hence differential

solvation due to the presence of water has a large impact on the IPs and acts in favor of the ionization.

Cluster Franck-Condon vertical energies (E^n_{FC}) for the $V^-(A) \leftarrow X^-(A)$ transition were calculated for clusters up to size 4, where the geometries employed are optimized nonionic clusters, presented in Chapter II. The differential solvation energy (ΔE^n_{solv}) is related to the cluster Franck-Condon energies as:

$$E^n_{FC} = E^0_{FC} + \Delta E^n_{solv}, \quad (1)$$

where E^0_{FC} is the Franck-Condon vertical excitation from the ground to the ion-pair state of HBr. Cluster Franck-Condon energies (Figure 22) and differential solvation energies (Figure 23) are shown along with the oscillator strengths (Figure 22) calculated for the transitions $C^1\Pi \leftarrow X^-\Sigma$ and $V^1\Sigma \leftarrow X^-\Sigma$. The vertical Franck-Condon excitation energy from the ground to the ion-pair state of $HBr(H_2O)_n$ decreases with cluster size increase and become approximately equal to the photoexcitation energy 5.34 eV used in [125] by cluster size 4.

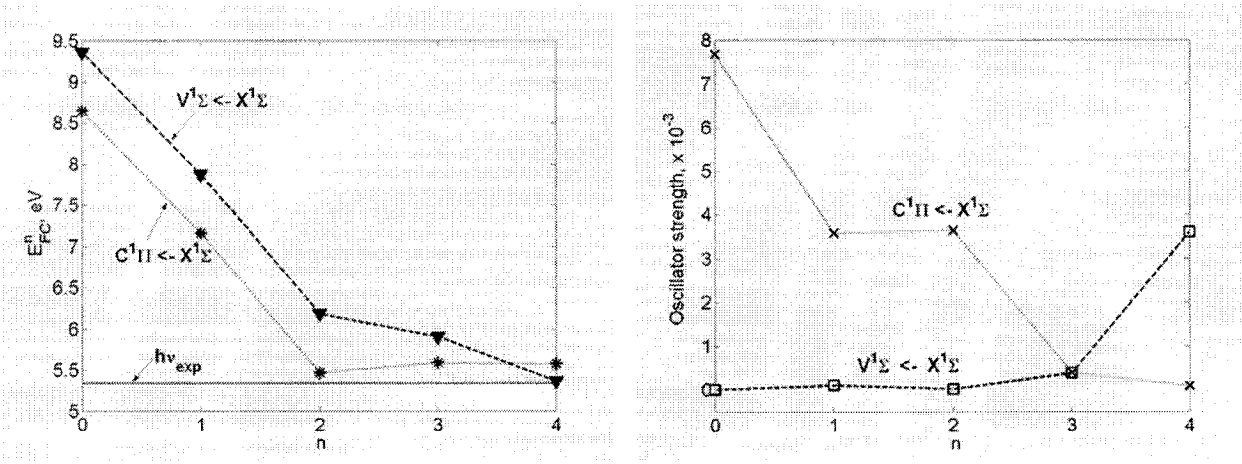

Figure 22: Franck-Condon energy for the ground to $C^1\Pi$ and ion-pair $V^1\Sigma$ state transitions along with corresponding oscillator strengths calculated with CAS-SCF/aug-cc-pVDZ. The solid line corresponds to the photoexcitation energy used in the experiment of Hurley *et al.* [125].

In their experimental studies of HBr photoionization in aqueous clusters, Castleman and co-workers report an increase in the ion signal following excitation of HBr-water clusters, which led them to conclude that complete ionization of hydrogen bromide in water clusters occurs only in the excited-valence (ion-pair) states of cluster size 5, and it is not likely to occur in the ground state. They assumed that the $\upsilon = 1$ vibrational level of the Rydberg $C^1\Pi$ was first reached upon excitation, and the ion-pair state was populated by internal conversion, in contrast to the gas phase scenario, because of the stabilization of the ion-pair state in water clusters [125].

Our calculation support the hypothesis that 4 water molecules are not enough to fully ionize HBr in its ground electronic state but that the $V^1\Sigma^+$ ion-pair state is accessible upon photoexcitation, either directly or internal conversion from the $C^1\Pi$ state. The origin of the discrepancy may lie in temperature effects. Further calculations of the oscillator strength related to optical accessibility of the $C\tilde{}(A)$ and $V\tilde{}(A)$ states for all clusters, but especially $HBr(H_2O)_4$, are underway.

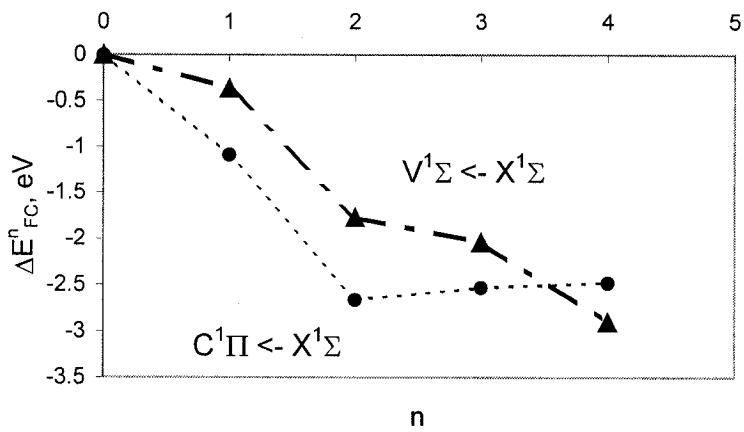

Figure 23. Differential solvation energy as a function of cluster size calculated with CAS-SCF/aug-cc-pVDZ.

IV.4. Conclusions

Some aspects of the photoionization of HBr in water clusters were investigated using the state-averaged complete active space self-consistent field method, paying particular attention to the potential energy and dipole moment curves of the lowest Rydberg and ion-pair excited states, and vertical Franck-Condon excitation energies. Analysis of the dipole moments in the ground and ion-pair state potentials were used to confirm the nature of these states for both HBr and $HBr(H_2O)$ clusters. A single water molecule stabilizes the very polar HBr ion-pair state by 1.02 eV, while stabilization is less significant for the ground and the Rydberg $C^{\sim}(A")$ states (0.19 and 0.34 eV, respectively). As a result of differential solvation the gap between the Rydberg and ion-pair states decreases to 0.1eV for $HBr(H_2O)$, compared to that for HBr (0.73 eV), implying that the ion-pair state may eventually become energetically accessible for larger clusters photoexcited to the $C^{\sim}(A")$ state through internal conversion. Further analysis shows that, the increased differential solvation, the vertical Franck-Condon energy for the ground to ion-pair state transition becomes approximately equal to the photoexcitation photon energy employed in the cluster experiments by cluster size 4. As inferred from experiments, combined with our previous analysis of ground-state $HBr(H_2O)_n$ clusters (Chapter II), this leads us to conclude that ground-state HBr is not fully ionized in water clusters up to size 4, but it ionizes in the excited ion-pair state upon photoexcitation, as 4 water molecules render this state energetically stabilized and thereafter optically accessible. Our assumption is based on the shift of both excited $C^{\sim}(A")$ and ion-pair $V^{\sim}(A')$ state and we predict that for larger clusters these two states will alternate leading

to full accessibility of the ion pair state. Thus the hydrogen bromide-water clusters excited to the C˜(A'') state will reach the V˜(A') state via internal conversion.

Chapter V.

General Conclusions

The main objective of this thesis was to further our understanding of the molecular interactions and mechanisms that govern ground and excited-state ionization of strong acids such as hydrogen halides in aqueous clusters. This was primarily motivated by recently reported experimental studies of HBr photoionization in small water clusters [34], a thorough interpretation of which needs further theoretical insight treatment. This thesis then reports **(1)** an investigation of the bonding structure and infrared spectra of ground-state $HX(H_2O)_n$ clusters [X=Cl, Br; n=0-4] (Chapter II), **(2)** high-level calculations of the gas-phase HBr electronic (excited) states (Chapter III), and **(3)** a preliminary account of the $HBr(H_2O)_n$ electronic excited states and the implications for photoionization (Chapter IV).

The ground electronic states of $HX(H_2O)_n$ clusters were characterized in the literature in terms of the relative stabilities of different conformations. Chapter II of this thesis describes a compilation of the information for relative stabilities of non-ionized and ionized clusters at CCSD(T)/aug-cc-pVTZ level of theory, with calculated infrared spectroscopic properties, geometrical parameters, and electronic density and its Laplacian. For the HX, $HX(H_2O)$ and $HX(H_2O)_2$ the presence of water results in increasing HX elongation of the bond distance, as well as a red shift of the acid stretching vibrational frequency consistent with the weakening of the covalent HX bond interaction, inferred from the analysis of the electron density and its Laplacian. The properties of these clusters were used as reference for assessment of ionized versus nonionized clusters for n = 3 and 4. At 3 waters both $HCl(H_2O)_3$ conformations are characterized with shared-shell interaction of H_a–X and H_w–O. Blue shift of the water bending modes was characteristic for deformation of the water cluster due to the presence of acid. Hence,

ionization cannot be achieved for $HCl(H_2O)_3$. On the contrary, accumulation of negative charge on the Br in $HBr(H_2O)_3$ D conformation, significant in comparison to the corresponding charges in the nonionized $HBr(H_2O)_3$ S conformation, the closed-shell interaction for H_a–Br, characteristic for ionic bonding and the disappearance of the H_a–Br vibrational mode but observation of H_3O^+ vibrational modes instead, are all indicators that $HBr(H_2O)_3$ D conformation is ionized complex. The $HX(H_2O)_4$ clusters exhibited reversed stability, more stable are the ionized, cyclic and diamond-like cluster. Closed-shell Laplacian contour for halide-water interaction, small values of the electron density and positive values for the Laplacian in the critical points of X...H_a and X...H_w were calculated in addition as evidence of the pure ionic interactions of the halide within the water network. The less stable pentamer and atop configurations in both $HX(H_2O)_4$ cluster exhibit covalent character of the H_a–X interaction and existing though large red shifted H_a–X frequency mode, identifying these clusters as nonionized.

The excited states of gas-phase HX have been studied extensively both experimentally and theoretically, especially the valence manifold contributing to the photodissociation has been described in detail in the literature in terms of potential energy curves, transition dipole moments and integral cross sections. However, due to strong perturbations between some of the low-lying Rydberg states and the ion-pair state of HBr, the rovibrational structure of those states and subsequently the photoionization of HBr still require investigation. The ion-pair state and neighboring excited states of gas-phase HBr calculated with the multi-reference configuration interaction method (MRCI/aug-cc-pVTZ) are discussed in Chapter III for all states up to the lowest ion-pair limit along with a complete list of the bound-state vibrational levels of the Rydberg

states. Calculated Franck-Condon energies were found to compare well with available experimental values. It was shown that spin-orbit coupling is significant for the ground and valence (repulsive) manifolds, as well as for the Rydberg $C^1\Pi$ and $E^1\Sigma$, and ion-pair $V^1\Sigma$ states. From the transition dipole moments calculated with inclusion of spin-orbit coupling, all $A^1\Pi$, $a^3\Pi$, and $t^3\Sigma$ states were found to be optically accessible and to contribute to the initial excitation from the ground state in HBr photodissociation, as reported earlier [92]. Including spin-orbit effects in the calculation of the low-lying Rydberg and ion-pair states was especially important due to their extensive perturbation at large internuclear separations and to explain the uneven distribution of the vibrational levels for these states. The ion-pair state is characterized by a two-well potential, with wells separated by a barrier of 16.2 kcal/mol, a value suggesting that a tunneling mechanism should be considered for gas-phase HBr photoionization, which could explain the low yield depending, on which vibrational level is reached in experimental studies.

Calculations of the excited states of $HBr(H_2O)_n$ were performed with the complete active space self-consistent field (CASSCF/aug-cc-pVDZ) method, as a suitable compromise between accuracy and computational cost. Finally, it was shown in Chapter IV that stabilization effects of water are most significant for the ion-pair $V^1\Sigma^+$ state, which is shifted down in energy by 1.02 eV for $HBr(H_2O)$ compared to gas-phase HBr, and thus approaches the $C^1\Pi$ state. This may explain the experimentally observed increase in the absorption cross section for larger clusters [34]. With cluster size increase, the Franck-Condon vertical excitation energies to the ion-pair state decrease, due to increasing differential solvation effects, and by cluster size 4, the Franck-Condon energy approaches almost exactly (5.32 eV) the experimental photoexcitation pump energy

(5.34 eV) [34]. This combined with the results of Chapter II, leads to the very important conclusion that, in the ground state, HBr forms stable ionized complexes with water in clusters containing fewer than four water molecules and it does fully ionize in the excited state upon photoexcitation.

This investigation of the electronic structure of $HX(H_2O)_n$ clusters, with the use of quantum chemical methods brought further insight into the nature of the underlying molecular interactions that govern the mechanism of ionization of strong acids, such as HCl and HBr, in the presence of a few water molecules. It was also clearly shown that solvation affects the electronic structure of the excited states of HBr, rendering the ionic channel possible upon photoexcitation, a finding that could have implications for precursor reactions to ozone depletion.

References

1. Arrhenius, S.A., *Z. Phys. Chem.,* **1887**, 1, 631.
2. Robertson, W.H. and Johnson, M.A., *Science,* **2002**, 298, 69.
3. Yarnell, A., *Chemical and Engineering News,* **2006**, 84, 12.
4. Lobet, S. and Dutzler, R., *Europ. Mol. Biol. Org. J.,* **2006**, 25, 24.
5. Weatherhead, E.C. and Andersen, S.B., *Nature,* **2006**, 441, 39.
6. Peter, T., *Annu. Rev. Phys. Chem.,* **1997**, 48, 785.
7. Molina, M.J. and Rowland, F.S., *J. Phys. Chem.,* **1975**, 79, 667.
8. Song-Miao, F. and Jacob, D.J., *Nature,* **1992**, 359, 522.
9. Crutzen, P., *Geophys. Res. Lett.,* **1974**, 1, 205.
10. Molina, M.J. and Rowland, F.S., *Nature,* **1974**, 249, 810.
11. Molina, M.J. and Rowland, F.S., *Geophys. Res. Lett.,* **1974**, 1, 309.
12. Abbatt, J.P.D. and Molina, M.J., *Annu. Rev. Energy Environ.,* **1993**, 18, 1.
13. Rowland, F.S., *Annu. Rev. Phys. Chem.,* **1991**, 42, 731.
14. Molina, M.J., Molina, L.T. and Kolb, C.E., *Annu. Rev. Phys. Chem.,* **1996**, 47, 327.
15. Galvez, O., Zoermer, A., Loewenschuss, A. and Grothe, H., *J. Phys. Chem. A,* **2006**, 110, 6472.
16. Solomon, S., Garcia, R.R., Rowland, F.S. and Wuebbles, D.J., *Nature,* **1986**, 321, 755.
17. Gertner, B.J. and Hynes, J.T., *Science,* **1996**, 271, 1563.
18. Gertner, B.J. and Hynes, J.T., *Faraday Discuss.,* **1998**, 110, 301.

19. Bianco, R. and Hynes, J.T., *Int. J. Quant. Chem.,* **1999**, 75, 683.

20. Bianco, R. and Hynes, J.T., *Acc. Chem. Res.,* **2006**, 39, 159.

21. Hanson, D.R. and Ravishankara, A.R., *J. Phys. Chem.,* **1992**, 96, 2682.

22. Delzeit, L., Powell, K., Uras, N. and Devlin, J.P., *J. Phys. Chem. B,* **1997**, 101, 2327.

23. Pursell, C.J., Zaidi, M., Thompson, A., Fraser-Gaston, C. and Vela, E., *J. Phys. Chem. A,* **2000**, 104, 552.

24. Amirand, C. and Maillard, D., *J. Mol. Str.,* **1988**, 176, 181.

25. Sadtchenko, V., Giese, C.F. and Gentry, W.R., *J. Phys. B,* **2000**, 104, 9421.

26. Andersson, P.U., Nagard, M.B. and Pettersson, J.B.C., *J. Phys. Chem. B,* **2000**, 104, 1596.

27. Mantz, Y.A., Geiger, F.M., Molina, L.T. and Molina, M.J., *J. Phys. Chem. A,* **2001**, 105, 7037.

28. Gertner, B.J., Peslherbe, G.H. and Hynes, J.T., *Isr. J. Chem.,* **1999**, 39, 273.

29. Conley, C. and Tao, F.-M., *Chem. Phys. Lett.,* **1999**, 301, 29.

30. Nauta, K. and Miller, R.E., *Science,* **2000**, 287, 293.

31. Okumura, M., *J. Chem. Phys.,* **1986**, 85, 2328.

32. Ayotte, P., Weddle, G.H. and Johnson, M.A., *J. Chem. Phys.,* **1999**, 110, 7129.

33. Abbatt, J.P.D., *Chem. Rev.,* **2003**, 103, 4783.

34. Hurley, S.M., Dermota, T.E., Hydutsky, D.P. and Castleman Jr, A.W., *Science,* **2002**, 298, 202.

35. Ando, K. and Hynes, J.T., *J. Mol. Liquids,* **1995**, 64, 25.

36. Ando, K. and Hynes, J.T., *J. Phys. Chem. B,* **1997**, 101, 10464.

37. Svanberg, M., Pettersson, J.B.C. and Bolton, K., *J. Phys. Chem. A,* **2000**, 104, 5787.

38. Mantz, Y.A., Geiger, F.M., Molina, L.T., Molina, M.J. and Trout, B.L., *Chem. Phys. Lett.,* **2001**, 348, 285.

39. Parcker, M.J. and Clary, D.C., *J. Phys. Chem.,* **1995**, 99, 14323.

40. Sobolewski, A.L. and Domcke, W., *J. Phys. Chem. A,* **2003**, 107, 1557.

41. Mebel, M.A. and Morokuma, J., *J. Phys. Chem.,* **1996**, 100, 2985.

42. Alikhani, M.E. and Silvi, B., *Phys. Chem. Chem. Phys.,* **2003**, 5, 2494.

43. Odde, S., Mhin, B.J., Lee, S., Lee, H.M. and Kim, K.S., *J. Chem. Phys.,* **2004**, 120, 9524.

44. Cabalero-Lago, E., *J. Chem. Phys.,* **2002**, 117, 3160.

45. Tachikawa, M., *Mol. Phys.,* **2002**, 100, 881.

46. Re, S., Osamura, Y., Suzuli, Y. and Schaefer III, H., F., *J. Chem. Phys.,* **1998**, 109, 973.

47. Lee, C. and Sosa, C., *J. Chem. Phys.,* **1996**, 104, 7081.

48. Milet, A., Struniewicz, C., Moszynski, R. and Wormer, P.E.S., *J. Chem. Phys.,* **2001**, 115, 349.

49. Nirmala, V. and Kolandaivel, P., *Z. Phys. Chem.,* **2004**, 218, 327.

50. Lobet, S.v. and Dutzler, R., *Europ. Mol. Biol. Org. J.,* **2006**, 25, 24.

51. Yarnell, A., *Chem. Eng. News,* **2006**, 84, 12.

52. Girardet, C. and Toubin, C., *Surf. Sci. Rep.,* **2001**, 44, 159.

53. Molina, M.J., *The Chemistry of the Atmosphere*, **1994**, Oxford.

54. Gertner, B.J. and Hynes, J.T., *Science,* **1996**, 271, 1563.

55. Delzeit, L., Powell, K., Uras, N. and Devlin, P.J., *J. Phys. Chem. B,* **1997**, 101, 2327.

56. Pursell, C.J., Zaidi, M., Thompson, A., Fraser-Gaston, C. and Vela, E., *J. Phys. Chem. A,* **2000**, 104, 552.

57. Andersson, P.U., Nagard, M.B. and Pettersson, J.B.C., *J. Phys. Chem. B,* **2000**, 104, 1596.

58. Sandorfy, C., *The Hydrogen bond : recent developments in theory and experiments*, ed. C. Sandorfy. Vol. 2, **1976**: Elsevier.

59. Bader, R.F.W., *Atoms in Molecules - A Quantum Theory*, **1990**: Oxford University Press, New York 1990.

60. Popelier, P., *Atoms in Molecules, An Introduction*, **2000**: Prentice Hall.

61. Parthasarathi, R., Sabramanian, V. and Sathyamurthy, N., *J. Phys. Chem. A,* **2006**, 110, 3349.

62. Head-Gordon, M., Pople, J.A. and Frisch, M.J., *Chem. Phys. Lett.,* **1988**, 153, 503.

63. Frisch, M.J., Head-Gordon, M. and Pople, J.A., *Chem. Phys. Lett.,* **1990**, 166, 275.

64. Saebo, S. and Almlof, J., *Chem. Phys. Lett.,* **1989**, 154, 83.

65. Dunning, J., T.H., *J. Chem. Phys.,* **1989**, 90, 1007.

66. Woon, D.E. and Dunning, J., T.H., *J. Chem. Phys.,* **1993**, 98, 1358.

67. Bergner, A., Dolg, M., Kuechle, W., Stoll, H. and Preuss, H., *Mol. Phys.,* **1993**, 80, 1431.

68. Martin, J.M.L. and Sundermann, A., *J. Chem. Phys.,* **2001**, 114, 3408.

69. Gopalakrishnan, S., Liu, D. and Allen, H.C., *Chem. Rev.*, **2006**, 106, 1155.

70. Chaban, G.M., Benny Gerber, R. and Janda, K.C., *J. Phys. Chem. A,* **2001**, 105, 8323.

71. Clabo Jr., D.A., Allen, W.D., Remington, R.B., Yamaguchi, Y. and Schaefer, H.F., *Chem. Phys.*, **1988**, 123, 187.

72. Barone, V., *J. Chem. Phys.*, **2005**, 122, 014108.

73. Gaussian 03, R.C., Frisch, M. J.; Trucks, G. W.; Schlegel, H. B.; Scuseria, G. E.; Robb, M. A.; Cheeseman, J. R.; Montgomery, Jr., J. A.; Vreven, T.; Kudin, K. N.; Burant, J. C.; Millam, J. M.; Iyengar, S. S.; Tomasi, J.; Barone, V.; Mennucci, B.; Cossi, M.; Scalmani, G.; Rega, N.; Petersson, G. A.; Nakatsuji, H.; Hada, M.; Ehara, M.; Toyota, K.; Fukuda, R.; Hasegawa, J.; Ishida, M.; Nakajima, T.; Honda, Y.; Kitao, O.; Nakai, H.; Klene, M.; Li, X.; Knox, J. E.; Hratchian, H. P.; Cross, J. B.; Bakken, V.; Adamo, C.; Jaramillo, J.; Gomperts, R.; Stratmann, R. E.; Yazyev, O.; Austin, A. J.; Cammi, R.; Pomelli, C.; Ochterski, J. W.; Ayala, P. Y.; Morokuma, K.; Voth, G. A.; Salvador, P.; Dannenberg, J. J.; Zakrzewski, V. G.; Dapprich, S.; Daniels, A. D.; Strain, M. C.; Farkas, O.; Malick, D. K.; Rabuck, A. D.; Raghavachari, K.; Foresman, J. B.; Ortiz, J. V.; Cui, Q.; Baboul, A. G.; Clifford, S.; Cioslowski, J.; Stefanov, B. B.; Liu, G.; Liashenko, A.; Piskorz, P.; Komaromi, I.; Martin, R. L.; Fox, D. J.; Keith, T.; Al-Laham, M. A.; Peng, C. Y.; Nanayakkara, A.; Challacombe, M.; Gill, P. M. W.; Johnson, B.; Chen, W.; Wong, M. W.; Gonzalez, C.; and Pople, J. A.; Gaussian, Inc., Wallingford CT, 2004.

74. van Duijneveldt, F.B., van Duijneveldt-van de Rijdt, J.G.C.M. and van Lenthe, J.H., *Chem. Rev.*, **1994**, 94, 1873.

75. Xantheas, S., *J. Chem. Phys.*, **1996**, 104, 8821.

76. The AIMPAC suite of programs is available from Prof. R. F. W. Bader, M.U., Canada and from the AIMPAC website (www.chemistry.mcmaster.ca/aimpac).

77. Loncke, P.G. and Peslherbe, G.H., *J. Phys. Chem. A,* **2004**, 108, 4694.

78. Hubert, K.P. and Herzberg, G., *Molecular Spectra and Molecular Strucute IV: Constants of Diatomic Molecules*, **1979**: Van Nostrand Reinhold: New York.

79. Herzberg, G., *Spectra of Diatomic Molecules*. second ed. Molecular Spectra and Molecular Structure. Vol. I, **1950**: D. van Nostrand Company, Inc.

80. Herzberg, G., *Electronic Spectra and Electronic Structure of Polyatomic Molecules*. Molecular Spectra and Molecular Structure. Vol. III, **1966**: D. van Nostrand Company, Inc.

81. Lefebvre-Brion, H. and Field, R.W., *Perturbations in the Spectra of Diatomic Molecules*, **1986**, Orlando, Florida: Academic Press Inc.

82. Bettendorff, M. and Peyerimhoff, S.D., *Chem. Phys.*, **1982**, 66, 261.

83. Dishoeck, E.F.v., Hemert, M.C.v. and Dalgarno, A., *J. Chem. Phys.*, **1982**, 77, 3693.

84. Chapman, D.A., Balasubramanian, K. and Lin, S.H., *Chem. Phys.*, **1987**, 118, 333.

85. Callaghan, R. and Gordon, R.J., *J. Chem. Phys.*, **1990**, 93, 4624.

86. Baig, M.A., Hormes, J., Connerade, J.P. and Garton, W.R., *J. Phys. B: At. Mol. Phys.*, **1981**, 14, L147.

87. Ginter, D.S., Ginter, M.L. and Tilford, S.G., *J. Mol. Spectrosc.*, **1981**, 90, 152.

88. Ascenzi, D., Langford, S.R., Ashfold, M.N.R. and Orr-Ewing, A.J., *Phys. Chem. Chem. Phys.*, **2001**, 3, 29.

89. Kvaran, A., Logadottir, A. and Wang, H., *J. Chem. Phys.*, **1998**, 109, 5856.

90. Kvaran, A., Wang, H. and Logadottir, A., *J. Chem. Phys.*, **2000**, 112, 10811.

91. Peoux, G., Monnerville, M., Duhoo, T. and Pouilly, B., *J. Chem. Phys.*, **1997**, 107, 70.

92. Smolin, A., Vasyutinskii, O.S., Balint-Kurti, G. and Brown, A., *J. Phys. Chem. A*, **2006**, 110, 5371.

93. Alekseyev, A.B., Liebermann, H.-P., Buenker, R.J., Balakrishnan, N., Sadeghpour, H.R., Cornett, S.T. and Cavagnero, M.J., *J. Chem. Phys.*, **2000**, 113, 1514.

94. Freund, R.S., *High-Rydberg Molecules*, in *Rydberg States of Atoms and Molecules*, R.F.a.D. Stebbings, F. B., Editor. 1983, Cambridge University Press. p. 355.

95. Hollas, J.M., *Modern Spectroscopy*. third ed, **1996**: John Wiley & Sons Ltd.

96. Hurley, S.M., Zhong, Q. and Castleman Jr., A.W., *J. Chem. Phys.*, **2000**, 112, 4644.

97. Hurley, S.M.D., T. E.; Hydutsky, D. P.; Castleman Jr, A. W., *J. Chem. Phys.*, **2003**, 118, 9272.

98. Buenker, R.J. and Krebs, S., *The Configuration-Driven Approach for Multireference Configuration Interaction Calculation*, in *Recent Advances in*

Computational Chemistry, v.4, K. Hirao, Editor. 1999, World Scientific: Singapur, New Jersey, London, Hong Kong. p. 1.

99. Serrano-Andres, L. and Merchan, M., *J. Mol. Structure: THEOCHEM,* **2005**, 729, 109.

100. Knowles, P.J. and Werner, H.J., *Chem. Phys. Lett.,* **1988**, 145, 514.

101. Werner, H.J. and Knowles, P.J., *J. Chem. Phys.,* **1988**, 89, 5803.

102. MOLPRO is a package of ab initio programs written by H.-J. Werner, P.J.K., M. Schütz, R. Lindh, P. Celani, T. Korona, G. Rauhut, F. R. Manby, R. D. Amos, A. Bernhardsson, A. Berning, D. L. Cooper, M. J. O. Deegan, A. J. Dobbyn, F. Eckert, C. Hampel, G. Hetzer, A. W. Lloyd, S. J. McNicholas, W. Meyer, M. E. Mura, A. Nicklaß, P. Palmieri, R. Pitzer, U. Schumann, H. Stoll, A. J. Stone R. Tarroni, and T. Thorsteinsson.

103. Knowles, P.J. and Werner, H.J., *Chem. Phys. Lett.,* **1985**, 115, 259.

104. Werner, H.J. and Knowles, P.J., *J. Chem. Phys.,* **1985**, 82, 5053.

105. Timerghazin, Q.K., Koch, D.M. and Peslherbe, G.H., *J. Chem. Phys.,* **2006**, 124, 034313.

106. Peterson, K.A., *J. Chem. Phys.,* **2003**, 119, 11099.

107. Peterson, K.A., Figgen, D., Goll, H., Stoll, H. and Dolg, M., *J. Chem. Phys.,* **2003**, 119, 11113.

108. Dunning, J., T.H., *J. Chem. Phys.,* **1989**, 90, 1007.

109. Glukhovtsev, M.N., *J. Mo. Struct. THEOCHEM,* **1995**, 357, 237.

110. Moore, C.E., *Atomic Energy Levels*, **1971**, Washington, D. C.: U. S. Goverment Printing Office.

111. Regan, P.M., Langford, S.R., Orr-Ewing, A.J. and Ashfold, M.N.R., *J. Chem. Phys.*, **1999**, 110, 281.

112. Roy, R., *LEVEL 7.1: A Computer Program for Solving the Radial Schrodinger Equation for Bound and Quasibound Levels*: University of Waterloo Chemical Physics Research Report CP-642R.

113. Zhang, J., Riehn, C.W., Dulligan, M. and Wittig, C., *J. Chem. Phys.*, **1996**, 104, 7027.

114. Alexander, M.H., Li, X., Liyanage, R. and Gordon, R.J., *Chem. Phys.*, **1998**, 231, 331.

115. Alexander, M.H., Pouilly, B. and Duhoo, T., *J. Chem. Phys.*, **1993**, 99, 1752.

116. Matsumi, Y., Tonokura, K., Kawasaki, M. and Ibuki, T., *J. Chem. Phys.*, **1990**, 93, 7981.

117. Alekseyev, A.B., Liebermann, H.-P., Kokh, D.B. and Buenker, R.J., *J. Chem. Phys.*, **2000**, 113, 6174.

118. Balakrishnan, N., Alekseyev, A.B. and Buenker, R.J., *Chem. Phys. Lett.*, **2001**, 341, 594.

119. Wales, N.P.L., Buma, W.J., Lange, C.A.d. and Lefebvre-Brion, H., *J. Chem. Phys.*, **1996**, 105, 2978.

120. Drescher, M., Irrgang, R., Spieweck, M., Heinzmann, U., Cherepkov, N.A. and Lefebvre-Brion, H., *J. Chem. Phys.*, **1999**, 111, 10883.

121. Cvejanovic, S., Cubric, D. and Jureta, J., *J. Phys. B: At. Mol. Phys.*, **1987**, 20, 2589.

122. Nenner, I. and Beswick, J.A., *Handbook of Synchrotron Radiation*, ed. G.V. Marr. Vol. 2, **1987**, Amsterdam: Elsevier.

123. Horn, A.B., Chesters, M.A., McCoustra, M.R.S. and Sodeau, J.R., *J. Chem. Soc., Faraday Trans.*, **1992**, 88, 1077.

124. Gertner, B.J. and Hynes, J.T., *Faraday Discuss.*, **1998**, 110, 301.

125. Hurley, S.M., Dermota, T.E., Hydutsky, D.P. and Castleman Jr., A.W., *Science,* **2002**, 298, 202.

126. Zlatkova, S.Z. and Peslherbe, G.H., *J. Chem. Phys.*, **2006**, to be submitted.

127. Zlatkova, S.Z. and Peslherbe, G.H., *J. Phys. Chem. A,* **2006**, to be submitted.

128. Werner, H.-J. and Knowles, P.J., *J. Chem. Phys.*, **1985**, 82, 5053.

129. Knowles, P.J. and Werner, H.-J., *Chem. Phys. Lett.*, **1985**, 115, 259.

130. Peterson, K.A., Figgen, D., Goll, E., Stoll, H. and Dol, M., *J. Chem. Phys.*, **2003**, 119, 11113.

131. Kendall, R.A., Dunning, J., T.H. and Harrison, R.J., *J. Chem. Phys.*, **1992**, 96, 6769.

Appendix

1. Cartesian coordinates (in Å) of optimized geometries in their standard orientation, and total energy (in a.u.) for the stationary-state structures of $HX(H_2O)_n$ clusters (X = Cl, Br, n = 0 – 4), calculated at the MP2 level of theory with aug-cc-pVTZ basis for H,O, and Cl and the SDB-aug-cc-pVTZ basis set for Br.

HCl

Cl	0.000000	0.000000	0.070833
H	0.000000	0.000000	-1.204167

Total energy = -460.3151301

HBr

Br	0.000000	0.000000	0.002107
H	0.000000	0.000000	1.411893

Total energy = -13.9170905

$HCl{\cdot}H_2O$

O	1.951762	-0.000381	-0.088391
H	2.367584	0.766172	0.319471
H	2.378012	-0.759170	0.323185
Cl	-1.202840	0.000108	0.006854
H	0.088588	-0.005786	-0.052042

Total energy = -536.6535423

$HBr{\cdot}H_2O$

O	2.560071	-0.000280	-0.092380
H	2.953595	0.765103	0.339387
H	2.961833	-0.759602	0.342477
Br	-0.772829	0.000043	0.003248
H	0.653034	-0.004747	-0.056516

Total energy = -90.2541956

$HCl(H_2O)_2$

O	-1.663454	-1.148217	0.093748
O	-0.950516	1.521304	-0.107523
Cl	1.518599	-0.198465	0.001964
H	-0.720077	-1.361775	0.064368
H	-2.068075	-1.717086	-0.567935
H	-1.478231	0.703963	-0.033817
H	-1.201315	2.060665	0.648822
H	0.563269	0.703433	-0.034629

Total energy = -612.9968437

$HBr(H_2O)_2$

O	-2.163302	-1.223675	0.094267
O	-1.645612	1.490599	-0.108201
Br	1.094161	-0.068004	0.000835
H	-1.210327	-1.390766	0.068538
H	-2.535126	-1.803434	-0.577336
H	-2.094315	0.626941	-0.031370
H	-1.925126	1.996404	0.661626
H	-0.059434	0.815600	-0.039223

Total energy = -166.5974295

$HCl(H_2O)_3$ (cyclic)

O	-2.326491	-0.327595	-0.017569
O	-0.156586	-1.924269	0.018735
O	-0.807846	1.955023	0.015772
Cl	1.885307	0.159271	-0.053616
H	-2.918490	-0.319563	-0.774826
H	-1.901487	0.555392	-0.007713
H	-1.012710	-1.433556	0.004206
H	-0.171511	-2.454673	0.821715
H	0.092388	1.590933	-0.019994
H	-0.798221	2.565383	0.758978
H	0.987195	-0.836781	-0.006394

Total energy = -689.3436513

$HBr(H_2O)_3$ (cyclic)

O	-2.877528	-0.266473	-0.029189
O	-0.807397	-1.956760	0.024232
O	-1.330542	1.985315	0.020576
Br	1.425608	0.062033	-0.026996
H	-3.463682	-0.242508	-0.790719
H	-2.433087	0.607926	-0.011008
H	-1.632365	-1.408453	0.002200
H	-0.833624	-2.442647	0.855881
H	-0.435716	1.605607	-0.013220
H	-1.312487	2.591562	0.767179
H	0.338403	-0.979308	0.009600

Total energy = -242.9441695

$HCl(H_2O)_3$ (diamond-like)

O	-0.000085	-1.033061	1.155414
H	0.000020	0.347200	0.709286
H	-0.778480	-1.337671	0.651215
H	0.778338	-1.337804	0.651348
O	2.125627	-0.901103	-0.605398
H	3.082711	-0.887782	-0.512965
H	1.870274	0.024040	-0.729520
O	-2.125700	-0.900973	-0.605506
H	-3.082718	-0.887431	-0.512406
H	-1.870224	0.024133	-0.729653
Cl	0.000079	1.572730	0.053918

Total energy = -689.3376006

$HBr(H_2O)_3$ (diamond-like)

O	-1.571650	0.001102	1.045165
H	-0.509264	0.000231	0.933965
H	-1.769950	0.806795	0.477605
H	-1.771316	-0.804349	0.477779
O	-1.293428	-2.070922	-0.459109
H	-1.611458	-2.341581	-1.325614
H	-0.379293	-1.745306	-0.593929
O	-1.290109	2.072585	-0.459167
H	-1.607773	2.343196	-1.325824
H	-0.376434	1.745617	-0.593841
Br	1.179057	-0.000764	0.026707

Total energy = -242.9417823

$HCl(H_2O)_4$ (diamond-like)

O	1.821022	0.008442	-0.127808
H	1.355040	-0.711337	-0.685502
H	1.370304	0.881705	-0.420537
H	1.442928	-0.149495	0.817381
O	0.390925	2.032084	-0.657106
H	-0.457607	1.547389	-0.480239
H	0.279721	2.476642	-1.502657
O	0.349550	-1.726960	-1.252718
H	-0.486521	-1.294126	-0.931765
H	0.225850	-1.895461	-2.191508
O	0.557919	-0.269181	2.044832
H	-0.327526	-0.210750	1.600211
H	0.543526	-1.083397	2.557707
Cl	-1.700061	0.004927	0.069371

Total energy = -765.6927764

$HBr(H_2O)_4$ (diamond-like)

O	2.276618	0.009356	-0.079093
H	1.834598	-0.726778	-0.634164
H	1.839975	0.876978	-0.405822
H	1.878767	-0.126930	0.860333
O	0.901963	2.046832	-0.706832
H	0.029289	1.603731	-0.552950
H	0.840256	2.470481	-1.568416
O	0.885508	-1.781952	-1.224395
H	0.018325	-1.380238	-0.957909
H	0.816491	-1.969978	-2.165447
O	0.992196	-0.222375	2.089915
H	0.102426	-0.176157	1.657667
H	0.984071	-1.025386	2.620841
Br	-1.394128	0.001125	0.014546

Total energy = -319.299433

$HCl(H_2O)_4$ (cyclic/open book)

O	1.934264	1.214578	0.675239
H	1.034371	1.445749	0.353835
H	1.957519	1.511704	1.589575
O	2.051288	-1.324132	-0.058374
H	2.780617	-1.455970	-0.671390
H	2.132890	-0.392172	0.276158
O	-0.327657	-1.309155	-0.933905
H	0.643716	-1.400177	-0.613169
H	-0.934581	-1.556027	-0.179390
O	-1.960306	-1.108685	1.077210
H	-1.901115	-0.156837	0.852078
H	-2.900442	-1.310211	1.108926
Cl	-0.934456	1.400014	-0.461910
H	-0.507937	-0.267128	-0.945514

Total energy = -765.690193

$HBr(H_2O)_4$ (cyclic/open book)

O	-1.493608	-1.859447	0.790310
H	-0.574903	-1.617258	0.539025
H	-1.450985	-2.048361	1.732648
O	-2.839039	0.163686	-0.239532
H	-3.454905	-0.162320	-0.902728
H	-2.445022	-0.639207	0.196092
O	-0.789430	1.427784	-0.983969
H	-1.673191	0.961771	-0.718678
H	-0.475283	1.982593	-0.205676
O	0.440733	2.274676	1.119484
H	0.967072	1.452761	1.017868
H	1.083801	2.989872	1.157531
Br	1.301394	-0.561433	-0.210396
H	-0.074621	0.676719	-0.942560

Total energy = -319.296256

$HCl(H_2O)_4$ (pentamer)

O	-0.182326	-2.336672	0.194911
H	0.590371	-1.755157	0.092480
H	-0.035088	-2.793785	1.028094
O	-2.512886	-0.972005	-0.219966
H	-1.703803	-1.506672	-0.074762
H	-2.892052	-1.300943	-1.039352
O	-1.957773	1.653981	0.095144
H	-2.201297	0.709489	-0.036777
H	-2.469946	1.945179	0.854382
O	0.669357	2.124092	0.100629
H	-0.307168	1.958897	0.106904
H	0.828633	2.710766	-0.645752
Cl	2.267789	-0.268827	-0.096873
H	1.506948	0.847115	-0.004121

Total energy = -765.6873133

$HBr(H_2O)_4$ (a top)

Br	2.083760	-0.029088	-0.275341
H	0.988432	0.557639	0.450429
O	-3.175172	-0.902929	-0.838611
H	-2.500779	-1.333184	-0.276018
O	-1.167435	-1.738968	0.844410
H	-0.917685	-0.864929	1.186861
O	-0.581513	0.981050	1.340510
O	-2.477539	1.693888	-0.415384
H	-1.256268	1.356159	0.726280
H	-2.833576	0.808421	-0.639678
H	-4.013617	-1.296690	-0.592532
H	-0.361653	-2.083422	0.450599
H	-0.598199	1.519162	2.134857
H	-2.224982	2.090597	-1.251257

Total energy = -319.308306

$HBr(H_2O)_4$ (pentamer)

O	-0.628347	2.383487	-0.057132
H	0.114142	1.745658	-0.005811
H	-0.437064	2.912574	-0.837276
O	-2.910110	1.008082	0.160015
H	-2.094988	1.559093	0.067456
H	-3.342060	1.319671	0.960007
O	-2.433719	-1.551527	-0.161867
H	-2.628853	-0.583988	-0.021346
H	-2.866460	-1.791399	-0.986619
O	-0.012653	-2.221337	0.036496
H	-0.998917	-1.933998	-0.050750
H	0.107430	-2.606800	0.914619
Br	1.695983	0.106185	0.004121
H	0.666016	-1.286907	-0.004613

Total energy = -319.310647

2. Vibrational frequencies and corresponding intensities for the optimized geometries of $HX(H_2O)_n$ clusters (X = Cl, Br, n = 0 – 4), calculated at the MP2 level of theory with the aug-cc-pVTZ basis set for H, O, and Cl and the SDB-aug-cc-pVTZ basis set for Br. Frequencies ω_i are in cm^{-1}, intensities are km/mol and are given in parentheses. No scaling factor is applied to the frequencies. The molecular modes associated with the frequency are labeled as: "bend" (bending motion of water); "sym" (symmetric stretch of water); "asym" (asymmetric stretch of water); HB (motion of the acid-water complex associated with hydrogen bond formation); "H-Cl" and "H-Br" (stretching motion of the acid); "C" (complex combination of molecular modes);"$_{sym}$p" (symmetric stretch of the in-plane O-H bonds in the pentamer structure); "$_{asym}$d" (the asymmetric stretch of the dangling/out-of-plane O-H groups).

Molecule	HB Frequencies (Intensities)	Acid Frequencies (Intensities)	Water Frequencies (Intensities)
H_2O	–	–	ω_{bend} = 1624.13 (72.60)
			ω_{sym} = 3860.53 (9.65)
			ω_{asym} = 3989.22 (76.19)
HCl	–	$\omega_{H\text{-}Cl}$ = 3048.15 (53.76)	–
$HCl{\cdot}H_2O$	ω_{HB} = 152.32 (30.21)	$\omega_{H\text{-}Cl}$ = 2814.06 (695.93)	ω_{bend} = 1624.10 (71.67)
	ω_{HB} = 184.34 (189.61)		ω_{sym} = 3845.87 (24.87)
	ω_{HB} = 189.03 (6.21)		ω_{asym} = 3972.96 (104.12)
	ω_{HB} = 498.41 (51.46)		
	ω_{HB} = 607.11 (39.66)		
$HCl(H_2O)_2$	ω_{HB} = 89.36 (5.84)	$\omega_{H\text{-}Cl}$ = 2562.00 (1079.84)	ω_{bend} = 1630.73 (84.61)
	ω_{HB} = 167.08 (117.95)		ω_{bend} = 1644.25 (30.51)
	ω_{HB} = 186.58 (17.47)		ω_{sym} = 3660.36 (331.11)
	ω_{HB} = 209.24 (9.73)		ω_{sym} = 3798.71 (96.89)
	ω_{HB} = 241.74 (79.22)		ω_{asym} = 3925.08 (125.39)
	ω_{HB} = 267.65 (71.27)		ω_{asym} = 3947.05 (147.59)
	ω_{HB} = 350.37 (122.69)		
	ω_{HB} = 422.83 (105.72)		
	ω_{HB} = 568.86 (86.65)		
	ω_{HB} = 680.75 (147.11)		
	ω_{HB} = 867.44 (41.46)		
$HCl(H_2O)_3$ (cyclic)	ω_{HB} = 37.97 (1.00)	$\omega_{H\text{-}Cl}$ = 2259.85 (1846.35)	ω_{bend} = 1643.15 (61.55)
	ω_{HB} = 66.25 (1.11)		ω_{bend} = 1655.94 (45.82)
	ω_{HB} = 138.65 (4.99)		ω_{bend} = 1676.99 (21.21)
	ω_{HB} = 190.20 (26.36)		ω_{sym} = 3466.94 (711.48)
	ω_{HB} = 193.41 (93.72)		ω_{sym} = 3590.54 (646.12)
	ω_{HB} = 235.54 (38.54)		ω_{sym} = 3731.44 (340.66)
	ω_{HB} = 245.97 (117.12)		ω_{asym} = 3915.24 (107.05)
	ω_{HB} = 272.20 (66.77)		ω_{asym} = 3931.93 (110.86)
	ω_{HB} = 313.81 (41.02)		ω_{asym} = 3934.50 (149.91)
	ω_{HB} = 321.12 (99.51)		

	ω_{HB} = 421.72 (47.39)		
	ω_{HB} = 458.23 (23.43)		
	ω_{HB} = 538.59 (99.23)		
	ω_{HB} = 723.33 (24.44)		
	ω_{HB} = 796.29 (171.31)		
	ω_{HB} = 844.53 (96.54)		
	ω_{HB} = 1009.04 (35.31)		
$HCl(H_2O)_3$ (diamond-like)	ω_{HB} = 42.77 (9.52)	$\omega_{H\text{-}Cl}$ = 1926.40 (2099.88)	ω_{bend} = 1627.84 (77.19)
	ω_{HB} = 67.91 (8.97)		ω_{bend} = 1630.10 (111.61)
	ω_{HB} = 77.80 (2.02)		ω_{bend} = 1656.30 (40.94)
	ω_{HB} = 130.02 (43.80)		ω_{sym} = 3658.70 (146.20)
	ω_{HB} = 156.81 (151.92)		$\omega_{sym}C$ = 3807.48 (64.68)
	ω_{HB} = 176.75 (46.78)		ω_{sym} = 3808.02 (112.80)
	ω_{HB} = 205.19 (13.30)		ω_{asym} = 3744.90 (474.10)
	ω_{HB} = 222.90 (27.65)		ω_{asym} = 3951.51 (202.24)
	ω_{HB} = 229.40 (75.08)		ω_{asym} = 3952.91 (80.16)
	ω_{HB} = 267.90 (70.21)		
	ω_{HB} = 366.85 (88.66)		
	ω_{HB} = 403.13 (281.94)		
	ω_{HB} = 487.62 (64.63)		
	ω_{HB} = 641.51 (16.68)		
	ω_{HB} = 650.20 (314.44)		
	ω_{HB} = 959.63 (54.60)		
	ω_{HB} = 1093.48 (33.04)		
$HCl(H_2O)_4$ (pentamer)	ω_{HB} = 19.66 (2.97)	$\omega_{H\text{-}Cl}C$= 2147.33 (2269.10)	ω_{bend} = 1648.71 (59.18)
	ω_{HB} = 40.69 (0.14)		ω_{bend} = 1660.05 (49.01)
	ω_{HB} = 50.12 (0.03)		ω_{bend} = 1673.81 (27.82)
	ω_{HB} = 66.11 (1.95)		ω_{bend} = 1695.94 (29.68)
	ω_{HB} = 135.54 (6.48)		$\omega_{sym}p$ = 3402.28 (982.07)
	ω_{HB} = 181.71 (15.65)		$\omega_{sym}p$ = 3504.02 (949.99)
	ω_{HB} = 186.73 (71.49)		$\omega_{sym}p$ = 3575.84 (624.37)
	ω_{HB} = 219.60 (38.80)		$\omega_{sym}p$ = 3718.10 (401.84)
	ω_{HB} = 227.42 (120.22)		$\omega_{asym}d$ = 3913.20 (99.19)
	ω_{HB} = 259.63 (106.14)		$\omega_{asym}d$ = 3932.75 (102.10)
	ω_{HB} = 275.61 (110.58)		$\omega_{asym}d$ = 3933.06 (150.22)
	ω_{HB} = 311.81 (33.21)		$\omega_{asym}d$ = 3935.30 (96.62)
	ω_{HB} = 320.57 (71.48)		
	ω_{HB} = 337.56 (52.75)		
	ω_{HB} = 444.94 (25.86)		
	ω_{HB} = 471.52 (33.10)		

	ω_{HB} = 490.49 (40.28)		
	ω_{HB} = 561.70 (63.51)		
	ω_{HB} = 754.76 (11.88)		
	ω_{HB} = 811.15 (151.54)		
	ω_{HB} = 869.88 (97.61)		
	ω_{HB} = 918.22 (86.83)		
	ω_{HB} = 1034.00 (31.17)		
Molecule	**HB Frequencies (Intensities)**	**H_3O^+ Frequencies (Intensities)**	**Water Frequencies (Intensities)**
$\underline{HCl(H_2O)_4}$ (diamond-like)	ω_{HB} = 74.47 (8.36)	$\omega_{umbr}C$ = 1494.49 (486.27)	$\omega_{bend}C$ = 1632.03 (30.14)
	ω_{HB} = 80.85 (2.72)	$\omega_{bend}C$ = 1788.41 (30.91)	$\omega_{bend}C$ = 1642.98 (23.61)
	ω_{HB} = 110.66 (2.95)	$\omega_{bend}C$ = 1814.07 (39.81)	$\omega_{bend}C$ = 1661.32 (8.38)
	ω_{HB} = 184.35 (6.99)	$\omega_{asym}C$ = 2661.81 (1373.6)	$\omega_{sym}C$ = 3297.33 (1189.92)
	ω_{HB} = 195.63 (16.19)	$\omega_{asym}C$ = 2735.13 (1242.5)	$\omega_{sym}C$ = 3324.14 (1075.81)
	ω_{HB} = 259.23 (40.41)	$\omega_{sym}C$ = 2948.50 (946.60)	$\omega_{sym}C$ = 3382.79 (1268.46)
	ω_{HB} = 263.35 (56.47)		ω_{asym} = 3911.11 (131.32)
	ω_{HB} = 289.31 (3.34)		ω_{asym} = 3918.85 (72.69)
	ω_{HB} = 302.26 (68.30)		ω_{asym} = 3920.62 (145.21)
	ω_{HB} = 319.23 (129.01)		
	ω_{HB} = 336.05 (175.42)		
	ω_{HB} = 384.16 (10.83)		
	ω_{HB} = 444.89 (41.72)		
	ω_{HB} = 484.43 (83.23)		
	ω_{HB} = 527.12 (132.57)		
	ω_{HB} = 700.01 (101.41)		
	ω_{HB} = 740.65 (73.62)		
	ω_{HB} = 823.53 (28.77)		
	ω_{HB} = 847.86 (29.29)		
	ω_{HB} = 992.61 (104.03)		
	ω_{HB} = 1041.77 (50.09)		

Molecule	**HB Frequencies (Intensities)**	**H_3O^+ Frequencies (Intensities)**	**Water Frequencies (Intensities)**
$\underline{HCl(H_2O)_4}$ (cyclic)	ω_{HB} = 29.74 (1.69)	$\omega_{umbr}C$ = 1409.57 (463.30)	$\omega_{bend}C$ = 1638.10 (89.24)
	ω_{HB} = 72.47 (2.86)	$\omega_{bend}C$ = 1715.62 (13.53)	$\omega_{bend}C$ = 1650.02 (41.04)
	ω_{HB} = 86.82 (4.73)	$\omega_{bend}C$ = 1732.17 (129.85)	$\omega_{bend}C$ = 1669.02 (27.50)
	ω_{HB} = 149.25 (16.58)	$\omega_{asym}C$ = 2216.44 (2284.9)	$\omega_{sym}C$ = 3342.78 (1216.38)
	ω_{HB} = 182.02 (9.79)	$\omega_{asym}C$ = 2807.51 (1620.2)	$\omega_{sym}C$ = 3522.16 (860.18)
	ω_{HB} = 234.00 (6.99)	$\omega_{sym}C$ = 3298.91 (476.22)	$\omega_{sym}C$ = 3595.02 (505.81)
	ω_{HB} = 236.00 (101.33)		ω_{asym} = 3920.84 (117.47)
	ω_{HB} = 260.11 (78.71)		ω_{asym} = 3923.48 (152.56)
	ω_{HB} = 266.74 (90.05)		ω_{asym} = 3925.26 (81.26)
	ω_{HB} = 333.27 (27.39)		
	ω_{HB} = 350.86 (234.33)		
	ω_{HB} = 361.28 (22.24)		
	ω_{HB} = 401.33 (80.12)		
	ω_{HB} = 420.72 (17.58)		
	ω_{HB} = 524.35 (86.87)		
	ω_{HB} = 631.88 (114.51)		
	ω_{HB} = 688.55 (76.72)		
	ω_{HB} = 744.11 (32.39)		
	ω_{HB} = 765.66 (95.54)		
	ω_{HB} = 914.26 (51.43)		
	ω_{HB} = 1026.71 (89.29)		

Molecule	HB Frequencies (Intensities)	Acid Frequencies (Intensities)	Water Frequencies (Intensities)
H_2O	–	–	ω_{bend} = 1624.13 (72.60)
			ω_{sym} = 3860.53 (9.65)
			ω_{asym} = 3989.22 (76.19)
HBr	–	$\omega_{H\text{-}Br}$ = 2706.61 (16.82)	–
$HBr{\cdot}H_2O$	ω_{HB} = 126.59 (3.55)	$\omega_{H\text{-}Br}$ = 2518.11 (539.85)	ω_{bend} = 1625.04 (68.85)
	ω_{HB} = 181.41 (6.71)		ω_{sym} = 3840.13 (25.82)
	ω_{HB} = 189.49 (213.21)		ω_{asym} = 3967.42 (99.86)
	ω_{HB} = 434.62 (40.54)		
	ω_{HB} = 535.95 (26.12)		
$HBr(H_2O)_2$	ω_{HB} = 75.15 (4.29)	$\omega_{H\text{-}Br}$ = 2256.22 (1067.48)	ω_{bend} = 1630.24 (76.23)
	ω_{HB} = 153.24 (27.20)		ω_{bend} = 1644.06 (32.68)
	ω_{HB} = 163.83 (102.80)		ω_{sym} = 3654.39 (328.16)
	ω_{HB} = 208.20 (7.38)		ω_{sym} = 3799.57 (92.30)
	ω_{HB} = 235.54 (78.02)		ω_{asym} = 3920.86 (125.77)
	ω_{HB} = 265.89 (74.78)		ω_{asym} = 3945.59 (152.45)
	ω_{HB} = 343.50 (137.51)		
	ω_{HB} = 411.33 (92.90)		
	ω_{HB} = 530.60 (65.30)		
	ω_{HB} = 647.92 (136.00)		
	ω_{HB} = 844.82 (52.32)		
$HBr(H_2O)_3$ (cyclic)	ω_{HB} = 35.44 (0.73)	$\omega_{H\text{-}Br}$ = 1863.50 (2148.50)	ω_{bend} = 1639.76 (56.27)
	ω_{HB} = 58.58 (1.27)		ω_{bend} = 1652.49 (34.68)
	ω_{HB} = 118.71 (5.55)		ω_{bend} = 1674.63 (66.75)
	ω_{HB} = 153.12 (56.90)		ω_{sym} = 3432.97 (755.16)
	ω_{HB} = 192.60 (81.94)		ω_{sym} = 3579.53 (652.54)
	ω_{HB} = 234.00 (33.47)		ω_{sym} = 3724.84 (362.41)
	ω_{HB} = 250.48 (119.72)		ω_{asym} = 3906.16 (107.00)
	ω_{HB} = 276.34 (62.57)		ω_{asym} = 3931.10 (123.85)
	ω_{HB} = 309.69 (33.59)		ω_{asym} = 3931.73 (142.50)
	ω_{HB} = 326.13 (112.85)		
	ω_{HB} = 424.45 (50.37)		

	ω_{HB} = 460.08 (15.91)		
	ω_{HB} = 527.97 (98.63)		
	ω_{HB} = 701.46 (24.56)		
	ω_{HB} = 803.37 (147.23)		
	ω_{HB} = 843.16 (86.37)		
	ω_{HB} = 1020.21 (34.13)		
Molecule	**HB Frequencies (Intensities)**	**H_3O^+ Frequencies (Intensities)**	**Water Frequencies (Intensities)**
$HBr(H_2O)_3$ (diamond-like)	ω_{HB} = 66.58 (1.45)	$\omega_{umbr}C$ = 1361.38 (753.46)	ω_{bend} = 1624.59 (35.96)
	ω_{HB} = 126.16 (19.42)	ω_{bend} = 1712.27 (87.87)	ω_{bend} = 1635.51 (59.66)
	ω_{HB} = 127.57 (6.30)	ω_{bend} = 1732.58 (47.57)	ω_{sym} = 3581.80 (446.60)
	ω_{HB} = 184.36 (148.77)	ω_{asym} = 2202.42 (2054.7)	ω_{sym} = 3598.04 (621.55)
	ω_{HB} = 204.90 (24.32)	ω_{asym} = 3164.68 (1118.8)	ω_{asym} = 3926.94 (66.65)
	ω_{HB} = 232.81 (2.35)	$\omega_{sym}C$ = 3205.77 (433.58)	ω_{asym} = 3928.44 (213.56)
	ω_{HB} = 284.33 (96.43)		
	ω_{HB} = 360.04 (33.26)		
	ω_{HB} = 388.07 (0.38)		
	ω_{HB} = 424.25 (194.22)		
	ω_{HB} = 568.74 (242.07)		
	ω_{HB} = 584.63 (1.80)		
	ω_{HB} = 695.21 (24.82)		
	ω_{HB} = 699.23 (85.33)		
	ω_{HB} = 789.80 (53.33)		

Molecule	HB Frequencies (Intensities)	Acid Frequencies (Intensities)	Water Frequencies (Intensities)
$HBr(H_2O)_4$ (a top)	ω_{HB} = 20.63 (0.62)	$\omega_{H\text{-}Br}C$ = 2421.22 (756.55)	ω_{bend} = 1649.06 (68.80)
	ω_{HB} = 31.55 (1.03)		$\omega_{bend}C$ = 1658.71 (71.08)
	ω_{HB} = 51.22 (0.63)		ω_{bend} = 1664.91 (85.26)
	ω_{HB} = 80.10 (1.55)		ω_{bend} = 1690.55 (6.68)
	ω_{HB} = 129.35 (15.46)		ω_{symp} = 3360.85 (673.63)
	ω_{HB} = 196.75 (4.01)		ω_{symp} = 3497.04 (880.10)
	ω_{HB} = 224.08 (73.03)		ω_{symp} = 3559.05 (757.12)
	ω_{HB} = 233.61 (13.23)		ω_{symp} = 3684.03 (337.03)
	ω_{HB} = 245.82 (38.47)		ω_{asymd} = 3909.04 (109.15)
	ω_{HB} = 259.08 (94.26)		ω_{asymd} = 3917.04 (96.33)
	ω_{HB} = 279.27 (32.89)		ω_{asymd} = 3926.42 (95.87)
	ω_{HB} = 291.04 (211.98)		ω_{asymd} = 3935.76 (102.78)
	ω_{HB} = 317.17 (13.15)		
	ω_{HB} = 392.46 (26.04)		
	ω_{HB} = 429.98 (15.94)		
	ω_{HB} = 459.31 (12.97)		
	ω_{HB} = 465.89 (33.76)		
	ω_{HB} = 513.11 (13.82)		
	ω_{HB} = 574.43 (108.01)		
	ω_{HB} = 708.34 (192.13)		
	ω_{HB} = 812.61 (174.32)		
	ω_{HB} = 879.96 (135.68)		
	ω_{HB} = 1010.09 (14.87)		
$HBr(H_2O)_4$ (pentamer)	ω_{HB} = 16.99 (2.35)	$\omega_{H\text{-}Br}C$= 1545.84 (2412.83)	ω_{bend} = 1644.38 (46.93)
	ω_{HB} = 39.83 (0.22)		$\omega_{bend}C$ = 1662.81 (64.33)
	ω_{HB} = 42.09 (1.91)		$\omega_{bend}C$= 1683.25 (292.56)
	ω_{HB} = 66.72 (5.55)		$\omega_{bend}C$= 1710.15 (392.16)
	ω_{HB} = 105.41 (43.66)		ω_{symp} = 3332.32 (1108.29)
	ω_{HB} = 147.43 (49.89)		ω_{symp} = 3478.44 (949.11)
	ω_{HB} = 187.12 (54.01)		ω_{symp} = 3563.36 (680.75)
	ω_{HB} = 220.14 (6.07)		ω_{symp} = 3701.53 (451.12)
	ω_{HB} = 228.19 (170.46)		ω_{asymd} = 3898.05 (100.99)
	ω_{HB} = 264.65 (51.95)		ω_{asymd} = 3930.02 (150.76)
	ω_{HB} = 278.89 (145.73)		ω_{asymd} = 3931.49 (100.59)
	ω_{HB} = 324.22 (7.91)		ω_{asymd} = 3935.05 (99.85)
	ω_{HB} = 329.12 (44.15)		

	ω_{HB} = 345.78 (118.76)		
	ω_{HB} = 449.96 (26.07)		
	ω_{HB} = 479.51 (33.49)		
	ω_{HB} = 503.86 (40.02)		
	ω_{HB} = 549.31 (57.77)		
	ω_{HB} = 768.19 (16.25)		
	ω_{HB} = 821.64 (130.14)		
	ω_{HB} = 899.15 (102.21)		
	ω_{HB} = 942.35 (48.87)		
	ω_{HB} = 1084.91 (24.37)		

Molecule	**HB Frequencies (Intensities)**	**H_3O^+ Frequencies (Intensities)**	**Water Frequencies (Intensities)**
$\underline{HBr(H_2O)_4}$ (cyclic)	ω_{HB} = 28.63 (1.13)	$\omega_{umbr}C$ = 1432.63 (398.62)	$\omega_{bend}C$ = 1636.05 (70.27)
	ω_{HB} = 72.95 (4.28)	$\omega_{bend}C$ = 1726.22 (29.64)	ω_{bend} = 1644.23 (27.07)
	ω_{HB} = 78.63 (2.60)	$\omega_{bend}C$ = 1745.08 (77.25)	$\omega_{bend}C$ = 1670.60 (32.99)
	ω_{HB} = 137.29 (12.22)	$\omega_{asym}C$ = 2529.36 (2305.6)	$\omega_{sym}p$ = 3312.31 (1172.10)
	ω_{HB} = 160.94 (5.99)	$\omega_{asym}C$ = 2719.97 (1536.9)	$\omega_{sym}p$ = 3523.36 (888.40)
	ω_{HB} = 227.97 (21.57)	$\omega_{sym}C$ = 3168.32 (670.30)	$\omega_{sym}p$ = 3565.12 (590.84)
	ω_{HB} = 235.84 (81.00)		$\omega_{asym}d$ = 3915.91 (148.95)
	ω_{HB} = 266.06 (54.56)		$\omega_{asym}d$ = 3918.06 (114.48)
	ω_{HB} = 272.87 (98.06)		$\omega_{asym}d$ = 3920.97 (104.21)
	ω_{HB} = 319.16 (53.86)		
	ω_{HB} = 341.83 (40.77)		
	ω_{HB} = 362.02 (193.41)		
	ω_{HB} = 398.81 (61.41)		
	ω_{HB} = 410.07 (12.24)		
	ω_{HB} = 532.38 (76.37)		
	ω_{HB} = 611.78 (102.63)		
	ω_{HB} = 665.05 (67.14)		
	ω_{HB} = 752.34 (64.27)		
	ω_{HB} = 755.40 (57.78)		
	ω_{HB} = 934.69 (59.01)		
	ω_{HB} = 1037.51 (94.88)		

Molecule	HB Frequencies (Intensities)	H_3O^+ Frequencies (Intensities)	Water Frequencies (Intensities)
$\underline{HBr(H_2O)_4}$ (diamond-like)	ω_{HB} = 70.85 (7.26)	$\omega_{umbr}C$ = 1486.24 (488.93)	ω_{bend} = 1627.90 (26.84)
	ω_{HB} = 76.79 (2.41)	$\omega_{bend}C$ = 1789.47 (25.26)	ω_{bend} = 1636.10 (17.83)
	ω_{HB} = 96.99 (3.28)	$\omega_{bend}C$ = 1815.55 (33.72)	$\omega_{bend}C$ = 1651.63 (5.56)
	ω_{HB} = 163.74 (6.26)	ω_{asym} = 2679.13 (1378.84)	$\omega_{sym}p$ = 3349.11 (1064.89)
	ω_{HB} = 172.40 (8.10)	ω_{asym} = 2747.83 (1273.16)	$\omega_{sym}p$ = 3372.71 (956.44)
	ω_{HB} = 214.88 (25.05)	ω_{sym} = 2953.59 (897.20)	$\omega_{sym}p$ = 3417.91 (1348.37)
	ω_{HB} = 258.71 (80.53)		$\omega_{asym}d$ = 3906.95 (140.35)
	ω_{HB} = 282.62 (17.00)		$\omega_{asym}d$ = 3913.95 (80.03)
	ω_{HB} = 300.51 (37.45)		$\omega_{asym}d$ = 3915.74 (155.36)
	ω_{HB} = 313.52 (101.34)		
	ω_{HB} = 325.25 (185.80)		
	ω_{HB} = 375.20 (7.29)		
	ω_{HB} = 426.96 (22.88)		
	ω_{HB} = 465.02 (76.17)		
	ω_{HB} = 507.68 (137.73)		
	ω_{HB} = 668.96 (112.73)		
	ω_{HB} = 702.83 (78.88)		
	ω_{HB} = 775.82 (21.88)		
	ω_{HB} = 845.26 (25.57)		
	ω_{HB} = 987.88 (90.41)		
	ω_{HB} = 1039.04 (49.50)		